



HAL
open science

Synergistic effect of ionic liquid (IL) cation and anion inhibits negative difference effect on Mg in water - IL mixtures

D. Kurchavov, U. Rustambek, A. Ottochian, G. Lefèvre, A. Seyeux, Ilaria Ciofini, P. Marcus, V. Lair, P. Volovitch

► To cite this version:

D. Kurchavov, U. Rustambek, A. Ottochian, G. Lefèvre, A. Seyeux, et al.. Synergistic effect of ionic liquid (IL) cation and anion inhibits negative difference effect on Mg in water - IL mixtures. *Corrosion Science*, 2022, 209, pp.110723. 10.1016/j.corsci.2022.110723 . hal-03856355

HAL Id: hal-03856355

<https://hal.science/hal-03856355v1>

Submitted on 16 Nov 2022

HAL is a multi-disciplinary open access archive for the deposit and dissemination of scientific research documents, whether they are published or not. The documents may come from teaching and research institutions in France or abroad, or from public or private research centers.

L'archive ouverte pluridisciplinaire **HAL**, est destinée au dépôt et à la diffusion de documents scientifiques de niveau recherche, publiés ou non, émanant des établissements d'enseignement et de recherche français ou étrangers, des laboratoires publics ou privés.



Synergistic effect of ionic liquid (IL) cation and anion inhibits negative difference effect on Mg in water - IL mixtures

D. Kurchavov^a, U. Rustambek^a, A. Ottochian^b, G. Lefèvre^a, A. Seyeux^a, I. Ciofini^b, P. Marcus^a, V. Lair^a, P. Volovitch^{a,*}

^a Chimie ParisTech, PSL University, CNRS, Institut de Recherche de Chimie Paris (IRCP), F-75005 Paris, France

^b PSL University, Chimie ParisTech, CNRS UMR 8060, Institute of Chemistry for Life and Health Sciences, CSB2D team, 75005 Paris, France

ARTICLE INFO

Keywords:

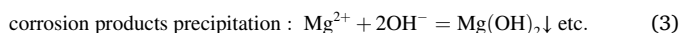
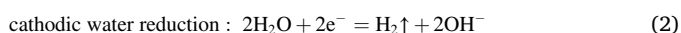
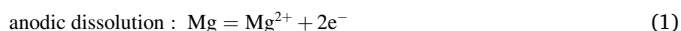
Mg alloys
Ionic liquids
PEG
Acetate
Negative difference effect (NDE)
Mechanisms

ABSTRACT

Strong Negative Difference Effect (NDE) is present on Mg alloys in [mPEG_nMPyr]ClO₄-H₂O and [BMPyr]AcO-H₂O but not in [mPEG_nMPyr]AcO-H₂O mixtures. The role of [mPEG_nMPyr]⁺ and its synergy with AcO⁻ in water-ionic liquids mixtures were characterized combining surface analysis by ToF-SIMS, surface and solution analysis by vibration spectroscopies and molecular dynamics simulations. The NDE was explained by the “free” water phase formation when Mg²⁺-ions expel water initially H-bonded with AcO⁻. Oxygen atoms of [mPEG_nMPyr]⁺ can bond the released water, inhibiting the NDE. Water transport can be reduced by a condensed film, formed by [mPEG_nMPyr]⁺ and AcO⁻ coordinated with Mg²⁺ and Al³⁺.

1. Introduction

The control of Mg reactivity is essential for multiple applications (engineering, biomedicine, energy storage, etc...) [1–3], because its poor corrosion resistance and high electrochemical reactivity define the life time of the devices. In aqueous electrolytes, corrosion of Mg is usually described as occurring via at least three parallel processes: anodic dissolution (reaction 1), cathodic hydrogen evolution reaction (HER) (reaction 2) and precipitation of corrosion products (reaction 3) [4].



While following the theory of electrochemical kinetics, i.e. the Butler-Volmer equation, the rate of cathodic reactions is expected to decrease exponentially with the increase of the applied anodic potential [5], Mg alloys in aqueous media exhibit the opposite behavior: HER is higher under anodic polarization if compared with spontaneous HER at open circuit potential, E_{oc} [6]. This phenomenon is referenced as “Negative Difference Effect” (NDE) or “anomalous” Hydrogen Evolution (HE). The uncontrolled corrosion processes under anodic polarization

could be particularly harmful for operating of Mg-based energy storage systems. Formed corrosion products passivate the metallic surface and increase the anode’s volume. Hydrogen reduction leads to a mass loss, which is significantly higher than what is calculated by Faraday’s law for a 2-electron transfer process and, therefore, to the decrease of the utilization efficiency (UE) of Mg anodes [7].

Numerous models have been proposed to elucidate the NDE in aqueous electrolytes (see for instance a recent review [8]), however there is no generally accepted universal theory describing its mechanism. The existing NDE theories include: partially protective surface film [9], uni-positive Mg⁺ ion [10,11], Mg hydride formation by a chemical reaction (MgH₂) [12,13], particle undermining [14], incomplete film containing univalent Mg⁺ ion [15], self-corrosion [16], or cathodic hydrogen evolution catalyzed by noble impurities, for instance segregated iron at grain boundaries, [17–21] or adsorbed surface species (Mg*H or Mg*OH) [22].

While the literature is abundant about the NDE in aqueous electrolytes, this effect is not discussed in organic electrolytes, such as ionic liquids (ILs). Usually, ILs consist of organic cations and organic or inorganic anions and are considered as green solvents with large electrochemical window, high flash point and low vapor pressure [23–25]. ILs seem therefore to be interesting electrolytes for Mg-based energy storage systems [26]. Corrosion rate of Mg anodes in non-aqueous electrolytes is usually significantly lower than in aqueous electrolytes

* Corresponding author.

E-mail address: polina.volovitch@chimieparistech.psl.eu (P. Volovitch).

<https://doi.org/10.1016/j.corsci.2022.110723>

Received 12 June 2022; Received in revised form 22 September 2022; Accepted 4 October 2022

Available online 7 October 2022

0010-938X/© 2022 The Author(s). Published by Elsevier Ltd. This is an open access article under the CC BY-NC-ND license (<http://creativecommons.org/licenses/by-nc-nd/4.0/>).

[27,28], while the electrolyte properties for ILs can be tuned by combining different cation and anion pairs. In the absence of water both HE on the anode and its passivation by Mg oxides and hydroxydes are not expected. Anhydrous electrolytes based on ILs, especially ILs containing etheric groups, were reported to support the most important reaction of secondary batteries, Mg stripping, with high coulombic efficiency [29,30].

Practical employment of anhydrous ILs is however limited due to their high viscosity and low conductivity (generally, few mS/cm or even less). Moreover, some ILs are unstable in humid atmospheres. At the same time, previous studies demonstrated that dilution of several sustainable ILs by small amounts of water can improve viscosity and conductivity without a significant decrease of the electrochemical potential stability window [31–35], which is expected to increase Mg reactivity. At the same time, the presence of water can lead to the negative effects discussed for aqueous electrolytes, such as the NDE. Indeed, extensive hydrogen evolution on Mg has been reported in some H₂O diluted ILs [36]. The effect however has never been studied in detail. In particular, the roles of the anion and the cation of the IL as well as the water content at which HE occurs remain unclear.

In our previous work [37], we have shown that, depending on the alloy and the IL's cation, the HE on Mg alloys can be very different for the water-IL mixtures with relatively high water content (10 wt%). In the mixture of aliphatically (butyl, -C₄H₉) substituted N-methylpyrrolidinium acetate ([BMPyr]AcO) with 10 wt% of H₂O, commercially pure Mg (CP Mg) and AZ61 revealed anomalous HE similar to that observed in aqueous electrolytes. However, the HE under anodic polarization decreased on CP Mg and was completely blocked on AZ61 in poly-etheric ((-O-CH₂-CH₂-)_n) substituted N-methylpyrrolidinium acetate ([mPEG_nPyr]AcO) with 10 wt% H₂O. In both electrolytes Mg(OH)₂ was detected after the experiment on CP Mg but not on AZ61 alloy. Several hypotheses were formulated in this work in order to explain the particular role of the cation and anion in these electrolytes and the role of Al alloying for the observed differences in the HE behavior. These hypotheses, which are verified in the present work, are detailed below.

1. Surface film hypothesis. The most intuitive idea, which could explain the NDE inhibition inherited from aqueous corrosion, is related to the modification of the metallic surface via formation of adsorbed films and/or dissolution of noble impurities or corrosion products. For example, for molecules containing carboxylate anions, a high inhibiting efficiency was assigned to the blocking of microgalvanic coupling due to the dissolution of metallic and oxide heterogeneities by the formation of soluble Mg and Fe complexes [38]. Their formation was confirmed by in situ vibration spectroscopy [39]. Adsorption of organic molecules on the precipitated Mg(OH)₂ crystals was proposed to be responsible for the inhibited crystal growth, leading to monocrystalline compact films, thus explaining the decrease of Mg corrosion by sodium salts of carboxylic acids [39] and sodium dodecyl sulfate (SDS) [40]. In the presence of 2, 5-pyridine carboxylate (PDCA) inhibition was correlated with the formation of a conjugated film coordinated by leached Mg²⁺ ions [39]. Corrosion inhibition of Mg was attributed to the formation of thin self-assembling adsorbed films in the presence of sodium diethyldithiocarbamate and sodium acetate [41], 6-ring organic compounds containing N-heteroatom [42], SDS [43] and sodium dodecylbenzenesulfate (SDBS) in ethylene glycol solutions [44]. These works considered a chemisorption of the molecules by polar groups and a hydrophobic barrier by the alkyl chains, limiting water diffusion to the surface. Similar inhibition mechanisms were reported for other surfactants based on carboxylic acids (R-COO⁻), phosphonic acids (R-PO₃²⁻), sulfonic (R-SO₃⁻) anions [45,46]. For Al-containing alloys, which surface can be enriched by Al and its oxides [47], specific interactions of organic molecules with Al could play an important role. Stable Al complexes with carboxylates were reported for pure Al [48], explaining high passivating effect of carboxylic acids on Al corrosion [49]. In alkaline solutions the inhibition efficiency increases with the number of carboxylic groups in the molecule [50] and with the carbon chain length

[51]. Inhibition action of quaternary amines on Al is also known [52].

Considering the above cited literature, one can expect that the surface films formed in water-IL mixtures can significantly differ from the surface films formed in aqueous solutions. Their composition and structure can be very complex and its composition and structure is difficult to predict. It can be adsorbed monolayers [44], surface complexes [34], thick low adherent condensed films, coordinated by leached cations [39], or even precipitated Mg(OH)₂ film modified by organic molecules [39,53]. A detailed surface analysis is therefore necessary to define the nature of the surface film and to verify the role of organic cations and anions in its inhibiting action. In the previous work [37] we have used Raman spectroscopy to access Mg(OH)₂ distribution and to prove the presence of both, anions and cations of IL in the humid surface film. The detailed analysis of the film composition provided by vibration spectroscopy needs however to be completed, in particular because its in-depth resolution is insufficient to verify the in-depth evolution of its chemical composition. Surface analytical techniques such as Time-of-Flight Secondary Ion Mass Spectrometry (ToF-SIMS) can be successfully applied to characterize the nature and structure of the surface films formed during corrosion and degradation of metallic materials and to understand the inhibition mechanisms, especially for Mg-alloys [54–57]. This technique is therefore selected to complete the surface characterizations of corroded materials in the present work.

2. Water "deactivation" by molecular interactions with organic species. Another hypothesis, explaining the NDE blocking in water – IL mixtures, can be more specific for organic solutions, in which water electrochemical reactivity can be affected by strong interaction between water and ILs moieties. For instance, hydrogen bonds, can alter the reaction of cathodic water reduction (2). Usually, water molecules interact predominantly with anions of ILs [58]. Among different anions studied in [58], the strongest hydrogen bonding (H-bonding) with water was found for trifluoroacetate (CF₃CO₂⁻). H-bonding between acetic anions and water [59,60] is well known, however, some evidences of weak interactions between water and aliphatic cation were also reported [61]. Insertion of etheric groups in the structure of organic cations can also be followed by the formation of hydrogen bonds between the oxygen of etheric groups and the water molecules [62]. In our previous work [63] we have demonstrated by ATR-FTIR and Raman spectroscopies, conductivity measurement and Molecular Dynamic (MD) simulations, that in mixtures with the studied ILs the water molecules can be involved in H-bonding with acetate anions and etheric groups of the cation. Molecular interactions between water and IL in the electrolyte used for an active anode could be complicated by the presence of leached by anodic dissolution metallic cations. For example, the carboxylate anion could form soluble complexes with leached Mg²⁺ [38] which can affect the interactions of carboxylates with water. Similarly, the dual function should be considered for the etheric substituted chain in the cation: water binding through intermolecular hydrogen bonds and complexation of released by anodic dissolution cations (Mg²⁺, Al³⁺ etc.).

Therefore, the roles of the IL cation and anion in the above discussed mechanisms (surface film formation, water bonding and complexation of metallic leached cations) need experimental and theoretical verification.

To sum up, the main objective of the present work is to understand the differences in the behavior of AZ61 and CP Mg in aliphatic and etheric substituted N-methylpyrrolidinium acetate based ILs and the role of the cation and the anion in the NDE and its inhibition. To reach this, the above formulated hypotheses of the mechanism of the NDE suppression via (i) formation of a surface film and (ii) the electrolyte modification were verified. In particular,

- 1) roles of etheric substituted cation and acetic anion in IL on HE reaction on Mg and their synergistic effect were verified by additional experiments in the mixture of water with etheric substituted cation and perchlorate anion [mPEG_nMPyr]ClO₄ - 10 wt% H₂O;

- surface films formed on different alloys after polarization in [mPEG_nMPyr]AcO - 10 wt% H₂O were characterized in detail with ToF-SIMS;
- molecular interactions in [mPEG_nMPyr]AcO - H₂O electrolyte in the presence of released Mg²⁺ were described with MD simulations and the results were corroborated with ATR-FTIR in order to discuss availability of “free water” for HE reaction.

2. Materials and methods

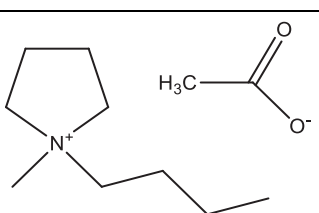
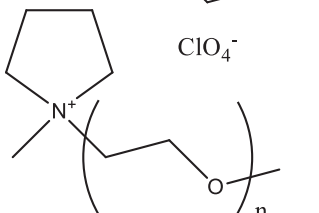
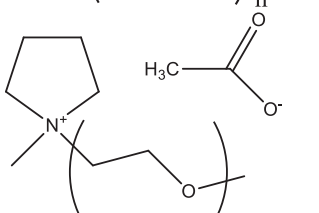
2.1. Materials choice

General procedure of the ILs synthesis is published in our previous work [63] and elsewhere [64,65]. Used chemicals are listed in [supplementary information](#). The present work considers the mixtures of 10 wt % water (Milli-Q water 18.2 Ω·cm) with three different ionic liquids presented in [Table 1](#).

In order to clarify if the NDE inhibition reported in [37] is governed only by the etheric substituted cation or a synergic effect of anion and cation is important, additionally to the previously discussed [BMPyr]AcO and [mPEG_nMPyr]AcO, similar to the reported in [37] experiments were conducted in the mixture of [mPEG_nMPyr]ClO₄-H₂O. Perchlorate anion was selected as an inorganic anion with low donor number and forming weak hydrogen bonds with water [58,66]. Its bonding with Mg-ions as well as H-bonding with H₂O molecules are supposed to be negligible.

The compositions of the alloys are presented in [Table 2](#). Commercial purity (CP) Al and Mg foils supplied by GoodFellow were used to verify the effect of alloying elements on the reactivity. Prior to electrochemical experiments the foils with the surface area of 1 × 1 cm² were grinded by 800, 1200, 2400, 4000 grits SiC polishing paper using absolute ethanol as a lubricant, rinsed with ethanol and dried.

Table 1
Graphical structures of used ILs.

Ionic liquid / short name	Tested effect	Graphical formula
1-N-butyl, 1-methylpyrrolidinium acetate / [BMPyr]AcO	Acetate anion	
1-poly(ethylene-glycol)-1-methylpyrrolidinium perchlorate / [mPEG _n MPyr]ClO ₄	Etheric cation	
1-poly(ethylene-glycol)-1-methylpyrrolidinium acetate / [mPEG _n MPyr]AcO	Synergy of acetate anion and etheric cation	

*n – means variable numbers of etheric groups found by MALDI-TOF, 4 ≤ n ≤ 16 with an average value <n> = 7.

Table 2
Chemical composition of metallic materials.

Sample name	Al ppm	Zn or Cu ppm	Mn ppm	Si ppm	Fe ppm	Ca ppm	Mg wt%
CP Mg	70	(Zn) < 20	170	50	280	–	Balance
AZ61	62.000	(Zn) 7.400	2.300	40	40	1.3	Balance
CP Al	Balance	(Cu) 0.3	–	0.8	0.3	–	1.2

2.2. Electrochemical experiments

Electrochemical experiments and setup design are described in [37]. A three-electrodes home-made electrochemical cell with aqueous AgCl/Ag (in saturated KCl) reference electrode and platinum rounded wire (S ≈ 1.23 cm²) counter electrode. The tested materials were used as working electrodes, the exposed area of 0.196 cm² was delimited by a PortHoles electrochemical mask. The working electrode chamber was filled by the IL electrolyte containing 10 wt% of water. The counter electrode chamber was filled with an aqueous solution containing 0.5 mol·l⁻¹ salts of Mg with the same anion as the anion of the tested IL (acetate or perchlorate). The working electrode and counter electrode compartments were separated by glass frits. The junction potential for perchlorate containing electrolyte [mPEG_nMPyr]ClO₄ - H₂O // 0.5 M Mg(ClO₄)₂-H₂O was measured as 86 mV. The junction potentials for acetate containing electrolytes were reported in [37].

For Mg alloys the electrochemical test was the same as in our previous work [37]. For CP Al the open circuit potential (E_{oc}) was significantly higher and the applied potential was E = +400 mV vs. E_{oc}. Three polarization cycles were applied after one hour of the E_{oc} measurement. One cycle consisted of 20 min of anodic polarization followed by 15 min of the E_{oc} measurement.

All the electrochemical experiments were conducted using Gamry 3000 potentiostat at room temperature and ambient atmosphere for at least 3 times. HE at open circuit and under anodic polarization was surveyed in situ by time lapse microscopy (TLM). HD USB camera with 2 MP CMOS detector and a 4000 K white LED enlightenment was coupled with the electrochemical cell. Images were automatically taken every 30 s

2.3. Chemical characterization by Raman spectroscopy

Raman spectra were collected with a Renishaw Confocal Raman Microscope InVia using red laser (HeNe, 633 nm, 17 mW power) and WiRE 4.2 software. Illumination and observation of the surface were performed through a microscope objective Leica of × 50 magnification and numerical aperture of 0.75. For the analysis of liquids, a droplet (approximately 15 μl) was placed on a Si-plate support and covered by a transparent glass. Laser beam was focused on the liquid phase. The exposure time was 10 s and 25 spectra were recorded for each sample. For each combination of the material and the electrolyte the characterizations were made at least on 3 different samples. The results were reproducible and for simplicity only one spectrum for each combination is shown in the next sections.

2.4. ToF-SIMS

The measurements were provided using a ToF-SIMS V spectrometer (ION-TOF GmbH, Muenster, Germany). The operating pressure in the chamber was around 10⁻⁹ mbar (ultra-high vacuum, UHV). Ion mass spectra (MS) and depth profiles were recorded. A Bi⁺ pulsed primary ions gun with a 45° angle to the surface was used for analysis. The surface sputtering was done using a Cs⁺ gun, also oriented with a 45° angle to the surface. Atomic and molecular ions (secondary ions), characteristic of the surface composition, were emitted and analyzed

using their mass to charge (m/z) ratio, measured by their time of flight to reach the detector.

Three types of analysis were carried out: positive and negative ions MS on the top surface and negative ions depth profile. Negative and positive MS were obtained by scanning a $500 \times 500 \mu\text{m}^2$ area using a 20 keV Bi^+ ion beam delivering 1.2 pA current. Negative ions depth profiles were conducted using the spectrometer in dual beam mode, meaning that Bi analyzing gun and Cs sputtering gun scan successively the surface. Thus, a $300 \times 300 \mu\text{m}^2$ crater was drilled by sputtering the surface with a 2 keV Cs^- ion beam delivering 100 nA. After each 1 s sputtering step, the analysis of the chemical composition was realized inside the crater by sputtering a $100 \times 100 \mu\text{m}^2$ area using a 20 keV Bi^+ ion beam delivering 1.2 pA current. The spectra were calibrated using at least five well identified peaks in the MS. Data treatment and post processing were carried out using the Ion-Spec software (version 6.9). The depth profiles represent the intensities of different components plotted versus sputtering time.

2.5. Modeling methodology

MD simulations were carried out with the Large-Scale Atomic/Molecular Massively Parallel Simulator (LAMMPS) package [67] of configurations prepared with the PACKMOL package [68]. The force field used is the plane GAFF distributed with Antechamber module [69,70] and Restained Electrostatic Potential (RESP) charges were assigned following the prescribed rules [71]. This means that an optimization with Gaussian16 [72] at Hartree Fock level of theory and the standard 6-31 * basis was performed.

Each simulation box contained one hundred of ions pairs and various number of water molecules and Mg^{2+} ions in order to replicate the experimental concentrations (see Table 1S in [supplementary information](#)). The electroneutrality of the systems was guaranteed by adding OH^- anions in a molar ratio $n(\text{OH}^-) / n(\text{Mg}^{2+}) = 2:1$. Addition of OH^- anions in such a ratio chosen because during Mg reactivity in aqueous electrolytes 2 OH^- anions are formed by the HE reaction (reaction 2) when 1 Mg^{2+} cation is formed by anodic Mg dissolution (reaction 1).

Each system was equilibrated for at least 1 ns long or even more. Simulations considered ambient conditions ($T = 298.15 \text{ K}$, pressure 1 atm) in a canonical ensemble (NVT) with volume mimicking the experimental densities. The production runs followed the micro-canonical (NVE) evolution for at least 1 ns, during which the total energy drift $\Delta E_{\text{tot}} / E_{\text{tot}}$ was checked to be always less than 10^{-6} in the worst case.

The structural characterization of all the systems was achieved observing the Radial Distribution Function (RDF) $G(r)$ of selected couples of species. Its definition is the following:

$$G_{\alpha\beta}(r) = \frac{1}{N_{\alpha} \cdot N_{\beta}} \left\langle \sum_{i,j}^{N_{\alpha}, N_{\beta}} \delta(r_{ij} - r) \right\rangle \quad (4)$$

where α and β stands for two species, the $\langle \dots \rangle$ indicates the usual ensemble average, and $\delta(x)$ is the Dirac delta function, r_{ij} is the distance between the i and j atoms whereas N_i indicates the number of i -species in the sample box.

3. Results

3.1. Typical NDE and not NDE behavior of Mg alloys in water-IL mixtures

To introduce the effect, we would like to illustrate two very different behaviors of Mg alloys in water / RTIL mixtures. Cathodic hydrogen production by reaction 2 in [mPEG_nPyrr]AcO with 10 wt% of H_2O electrolyte (Fig. 1) seems to follow “normal” behavior expected from classical electrochemical theories for both alloys. During the whole sequence (open circuits potential (OCP) measurement –

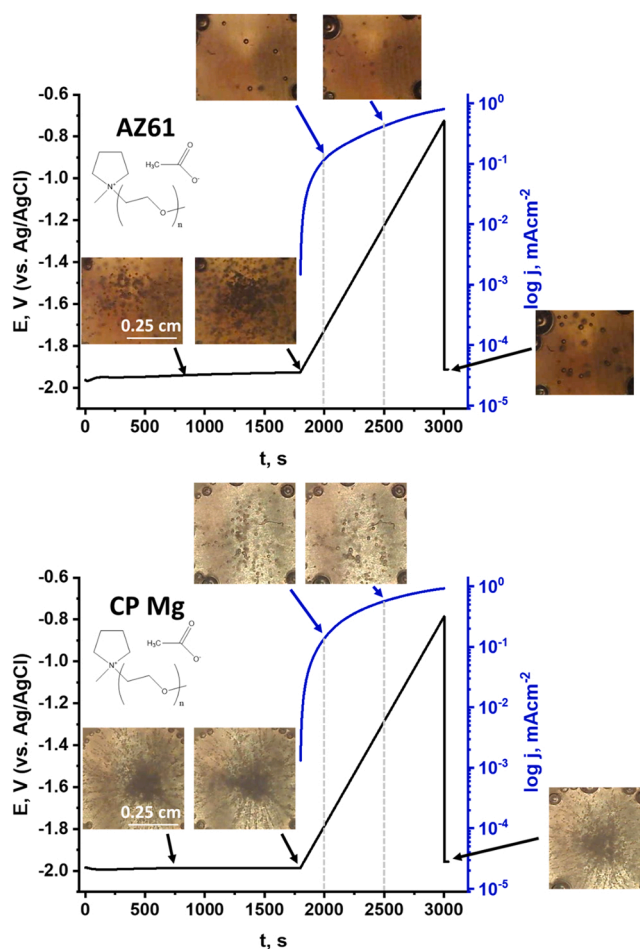


Fig. 1. Example of “normal” hydrogen evolution on AZ61 and CP Mg in [mPEG_nMPyr]AcO - H_2O mixture: gas formation decreases under anodic polarization.

potentiodynamic anodic polarization – OCP measurement) the tendency is: higher the anodic polarization level lower the cathodic gas formation. Moreover, it seems that anodic polarization is beneficial for cathodic inhibition (gas evolution at OCP is lower after polarization than on the initial surface). The tendency of the hydrogen gas evolution is opposite in [BMPyr]AcO with 10 wt% of H_2O electrolyte (Fig. 2). Only several bubbles form during initial immersion at OCP, much more intensive bubbling is visible under anodic polarization and gas formation reduces once polarization is stopped. Such a behavior (higher anodic polarization higher cathodic reactivity) is usual for Mg alloys in aqueous electrolytes and is typical for the NDE. It is also consistent with the hypothesis that anodic polarization in [BMPyr]AcO - water electrolyte activates cathodic reactivity of water on Mg alloys.

To conclude, simple observation of the surface during polarization curve measurement allows us to confirm the conclusions of our previous work [37] obtained from potentiostatic polarization experiments. Taking into account continuous surface evolution and possible effects of polarization potential on the surface state, relatively long potentiostatic polarization at fixed potential, rather than quick potentiodynamic polarization, seems to be more appropriate to form reproducible surface states. Therefore, the following sections concern the experiments and samples obtained using potentiostatic polarization procedures proposed in [37].

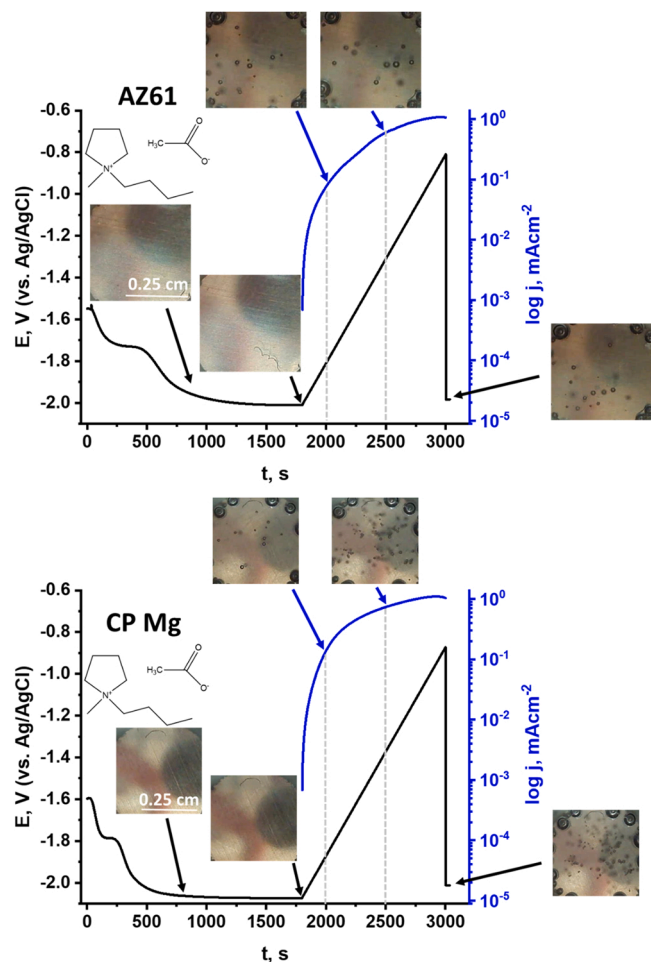


Fig. 2. Example of “anomalous” hydrogen evolution (NDE) on AZ61 and CP Mg in [BMPyr]AcO-H₂O mixture: gas formation increases under anodic polarization.

3.2. Magnesium alloys in [mPEG_nMPyr]ClO₄-H₂O mixture

3.2.1. Reactivity by electrochemical measurements and live imaging

In the [mPEG_nMPyr]ClO₄-H₂O mixtures, the E_{oc} reaches a quasi-steady state within 10 min at $E_{oc} = -1.81$ V vs. Ag/AgCl for CP Mg (Fig. 3a), and $E_{oc} = -1.64$ V vs. Ag/AgCl for AZ61 (Fig. 3b). Both values are significantly higher than the values, previously observed in [mPEG_nMPyr]AcO-H₂O mixtures ($E_{oc} \cong -2.0$ V) for the same materials [37].

Fig. 3 shows that the anodic current density stabilizes at 0.32 mAcm⁻² and 0.37 mAcm⁻² for CP Mg and AZ61 respectively under anodic polarization at applied potential $E = +0.7$ V vs E_{oc} and even higher at $E = +1$ V vs. E_{oc} (0.57 and 0.53 mAcm⁻² for CP Mg and AZ61 respectively). However, the surface of AZ61 seems to be active after anodic polarization, which was not the case in [mPEG_nMPyr]AcO-H₂O mixture [37]. The presence of acetic anion therefore significantly modifies anodic reactivity.

All the images Fig. 3a and b, independently on the alloy and if they are captured during the E_{oc} measurement (images I, II, IV, V, VI, VIII) taken under anodic polarization (images III and VII) display abundant hydrogen evolution. The HE is better visible in the dynamic mode (see videos in supplementary information available online) than on static images, in particular for the CP Mg, on which the bubbles are very tiny.

The images and video show also that no dark film formed on AZ61 in the [mPEG_nMPyr]ClO₄-H₂O mixture. The behavior in this electrolyte (HE under anodic polarization, no visible film on AZ61 alloy) is closer to

the previously observed in [BMPyr]AcO-H₂O and not in [mPEG_nMPyr]AcO-H₂O [37]. The modification of the anion is hence important.

3.2.2. Surface state after polarization by vibrational spectroscopy

Fig. 4 a represents Raman spectra recorded on the surface of CP Mg and AZ61 within the range 500–1600 cm⁻¹. Attribution of all the bands is detailed in Table S2 in supplementary information.

It can be seen from the figure, that all the characteristic signals associated with IL are present on the surfaces after the experiment. However, a slight modification of the spectra is observed at 780–860 cm⁻¹ region, attributed to C-O-C stretching vibrations of PEG-fragment of the cation [29,73]. On AZ61 this band is shifted to 794 cm⁻¹. On CP Mg this signal narrows and centers at 824 cm⁻¹. At the same time, low intensive new bands at 1070 cm⁻¹ and 1092 cm⁻¹ appear on AZ61 and CP Mg, respectively. These bands are between peaks 7 and 8 of the reference electrolyte (1049 and 1136 cm⁻¹) which are attributed to C-C, C-O and C-H bending vibrations of PEG (see Table S2 in supplementary information). Such modifications indicate interactions between the etheric groups and the surface (or the ions released during anodic polarization). Similar evolution was visible on both CP Mg and AZ61 in [mPEG_nMPyr]AcO-H₂O (new bands at 1099 cm⁻¹ and 1109 cm⁻¹ on AZ61 and CP Mg respectively) [37].

There is however a difference with the bulk electrolyte. New peaks at 1381 cm⁻¹ and 1370 cm⁻¹ are observed on AZ61 and CP Mg respectively. Their positions are very close to the values reported in the literature for the carboxylic group vibration (1360 – 1410 cm⁻¹). The electrolyte does not contain however carboxylic anion (see also the bulk electrolyte spectra in Fig. 4a). A hypothesis can be therefore proposed about a possible degradation of the PEG_n-substituted cation at Mg electrode. Indeed, it has been previously reported that etheric group in the presence of Mg²⁺-ions can undergo nucleophilic attack by OH⁻ ions and produce carboxyl, carbonyl or ester groups [74]. The fact that no other specific band has been observed can be interpreted as the formed compounds are probably present only as adsorbed species and other vibrations become inactive because of the symmetry modifications (see for instance [75]). The bands at 1381 cm⁻¹ and 1370 cm⁻¹ were however not observed on the surface of the same alloys after the electrochemical experiments in [mPEG_nMPyr]AcO-H₂O [37]. Therefore, considering the catalytic effect of leached Mg²⁺ on the nucleophilic attack of the [mPEG_nMPyr]ClO₄ by OH⁻-ion, the absence of such an attack in [mPEG_nMPyr]AcO-H₂O can be regarded as an indication of a protective action of acetate anion for etheric groups. The latter can be explained by a strong binding of Mg²⁺ in Mg(AcO)⁺ and Mg(OAc)₂ complexes, which were indeed detected in [mPEG_nMPyr]AcO-H₂O [37].

Similarly to acetate ILs [37], Fig. 4b evidences Mg(OH)₂ formation on the CP Mg and its absence on the AZ61 surfaces tested in water - IL mixtures. The peak position at 3710 cm⁻¹ indicates that Mg(OH)₂ is nanocrystalline [76]. These observations are also supported by ATR-FTIR spectroscopy (see supplementary information Fig. S1, Table S3).

3.3. Reactivity of aluminum in [mPEG_nMPyr]AcO-H₂O and [mPEG_nMPyr]ClO₄-H₂O mixtures

Our previous work [37] and the results, presented in Section 3.1. demonstrated significant differences in the behavior of CP Mg and AZ61 in [mPEG_nMPyr]AcO-H₂O. Although in both cases the NDE was not present, hydrogen evolution was not completely suppressed at the open circuit potential (OCP) on the CP Mg while it was on the AZ61 alloy. Additionally, a black film formed under polarization of the latter alloy. In order to understand the role of Al alloying in the inhibition of the HE, similar electrochemical experiments were repeated with CP Al in [mPEG_nMPyr]AcO-H₂O and [mPEG_nMPyr]ClO₄-H₂O. Fig. 5 displays the examples of the electrochemical response of the CP Al in [mPEG_nMPyr]AcO-H₂O and [mPEG_nMPyr]ClO₄-H₂O mixtures and live images taken during the experiments (IX-XIV). As it can be seen from the figure, the

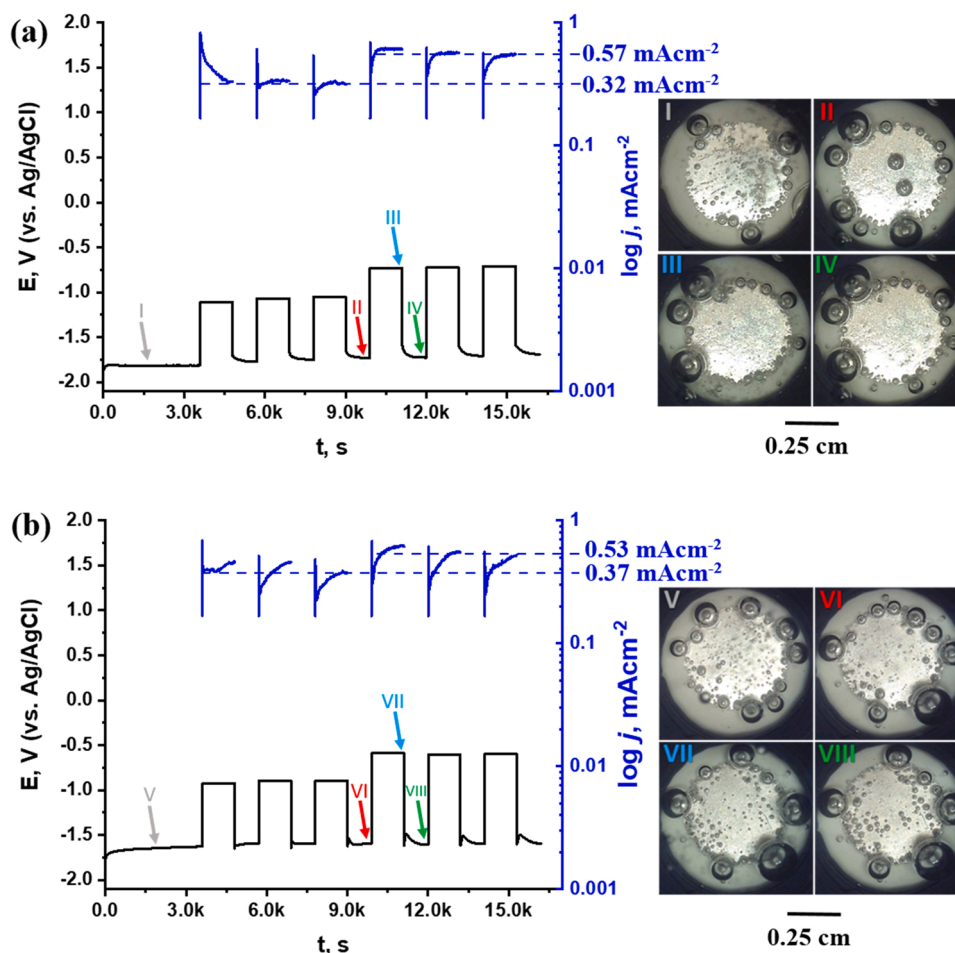


Fig. 3. Electrochemical response of (a) CP Mg and (b) AZ61 in $[m\text{PEG}_n\text{MPyr}]\text{ClO}_4\text{-H}_2\text{O}$ mixture and typical TLM images of the surface taken during the experiments. The time at which the selected images were taken is indicated by arrows (I-VIII) on the potential evolution curve.

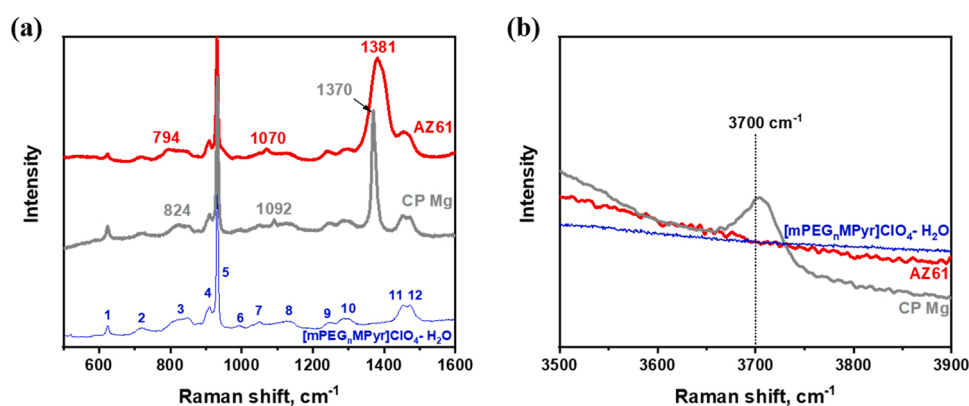


Fig. 4. Typical Raman spectra recorded on the surfaces of CP Mg and AZ61 (as indicated) after polarization in $[m\text{PEG}_n\text{MPyr}]\text{ClO}_4\text{-H}_2\text{O}$. The spectrum of $[m\text{PEG}_n\text{MPyr}]\text{ClO}_4\text{-H}_2\text{O}$ mixture is shown for comparison, peaks 1–12 are detailed in supplementary information.

reactivity of the CP Al surface is completely blocked both under E_{oc} conditions and under anodic polarization at $E = +0.4\text{ V}$ (vs. E_{oc}) in $[m\text{PEG}_n\text{MPyr}]\text{AcO-H}_2\text{O}$ (Fig. 5a).

In contrast, the CP Al surface remains reactive in $[m\text{PEG}_n\text{MPyr}]\text{ClO}_4\text{-H}_2\text{O}$ (Fig. 5b). Abundant hydrogen evolution under anodic polarization is also visible. These differences could be tentatively explained by the formation of stable Al-acetate complexes [49] adsorbed on the surface. This hypothesis is also supported by the Raman spectra recorded after the electrochemical experiment in $[m\text{PEG}_n\text{MPyr}]\text{AcO-H}_2\text{O}$ shown in

supplementary information. Raman shifts characteristic for acetic group vibrations (nearly 650 cm^{-1} , 917 cm^{-1} and 1407 cm^{-1}) are slightly shifted on the surface if compared to the electrolyte, indicating a possible chemisorption (see supplementary information Fig. S2).

Comparing the behavior of different materials in the $[m\text{PEG}_n\text{MPyr}]\text{AcO-H}_2\text{O}$ and $[m\text{PEG}_n\text{MPyr}]\text{ClO}_4\text{-H}_2\text{O}$ mixtures (Sections 3.1–3.3 and publication [37]), it is clear that for all materials the HE in the water – IL mixtures is controlled not only by the etheric substitution in the IL cation, but also by a synergistic effect of the etheric substituted cation

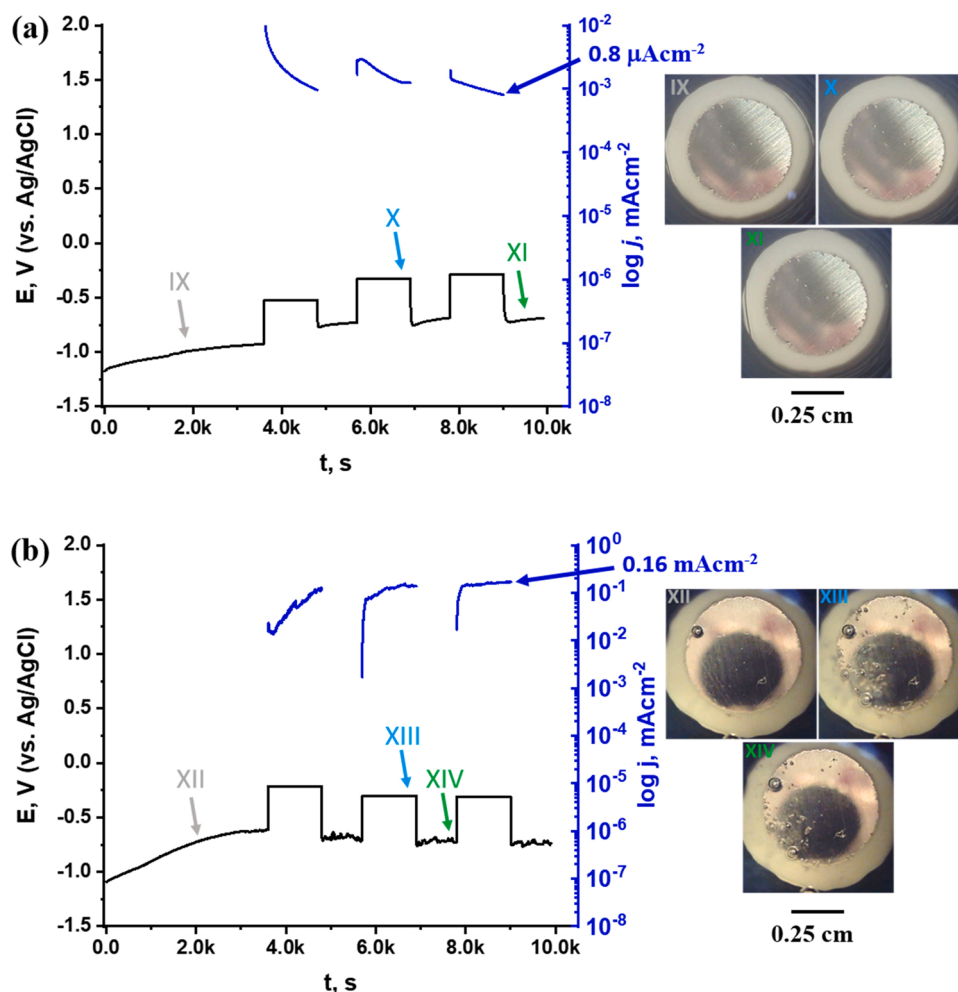


Fig. 5. Electrochemical response of CP Al in (a) $[m\text{PEG}_n\text{MPyr}]\text{AcO-H}_2\text{O}$ and (b) $[m\text{PEG}_n\text{MPyr}]\text{ClO}_4\text{-H}_2\text{O}$ mixtures and typical TLM images of the surface. The moments at which the selected images were taken are indicated on the potential evolution curve.

and acetate anions.

3.4. ToF-SIMS analysis of the surface films formed in $[m\text{PEG}_n\text{MPyr}]\text{AcO-H}_2\text{O}$ after potentiostatic polarization experiment

Positive and negative ion mass spectra of the surfaces after the electrochemical experiments in $[m\text{PEG}_n\text{MPyr}]\text{AcO-H}_2\text{O}$ are presented in [supplementary information](#) in Figs. S3, S4. The positions of the peaks in the positive ion MS mainly reflected the presence of $[m\text{PEG}_n\text{MPyr}]^+$ cation. The interpretation of the negative ion MS was more complex. The proposed structures and the corresponding masses are detailed in the [supplementary information](#) (Tables S4, S5). Briefly, the presence of carboxylate and etheric complexes was confirmed on the top surface, which is consistent with the results of Raman spectroscopy.

In depth organization of the film was studied from the negative ions depth profiles of selected ions shown in Figs. 6 and 7.

Specifically, the signals of MgO^- ($m/z = 39.97$), AlO^- ($m/z = 42.97$), $\text{MgO}(\text{OH})^-$ ($m/z = 57$) and OH^- ($m/z = 17$) can be used to detect oxides and hydroxides, the signal of CN^- ($m/z = 26$) is a marker of N heteroatom in the cation. Etheric groups are revealed by the C_2O^- ($m/z = 39.99$) fragment and specific complexes can be also verified by the fragments MgAcO^- ($\text{Mg}(\text{CH}_3\text{COO})^-$, $m/z = 83$) and $\text{C}_2\text{H}_4\text{MgO}^-$ ($m/z = 68$), $\text{Mg}(\text{AcO})_2^-$ ($\text{Mg}(\text{CH}_3\text{COO})_2^-$, $m/z = 141$), $\text{Al}(\text{AcO})_3^-$ ($\text{Al}(\text{CH}_3\text{COO})_3^-$, $m/z = 204$) and several specific fragments shown in Fig. 6 (these fragments have numbers 2 and 5 in Table S4 in [supplementary information](#), which details the MS peaks attribution).

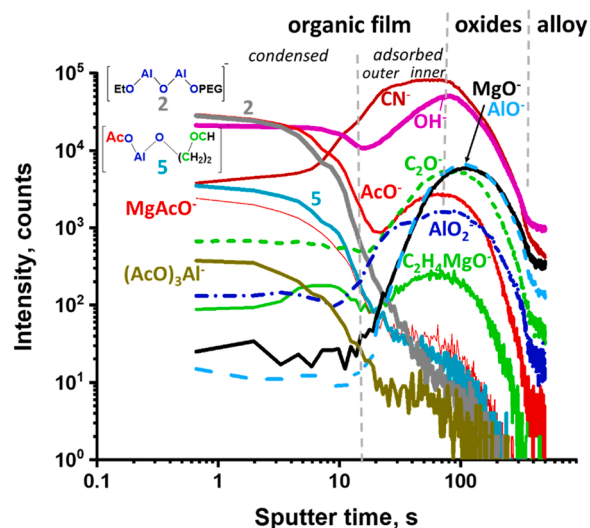


Fig. 6. Typical ToF-SIMS negative ions depth profile obtained after electrochemical experiments in $[m\text{PEG}_n\text{MPyr}]\text{AcO-H}_2\text{O}$ electrolyte on AZ61. Tentative positions of the interfaces are shown by vertical lines.

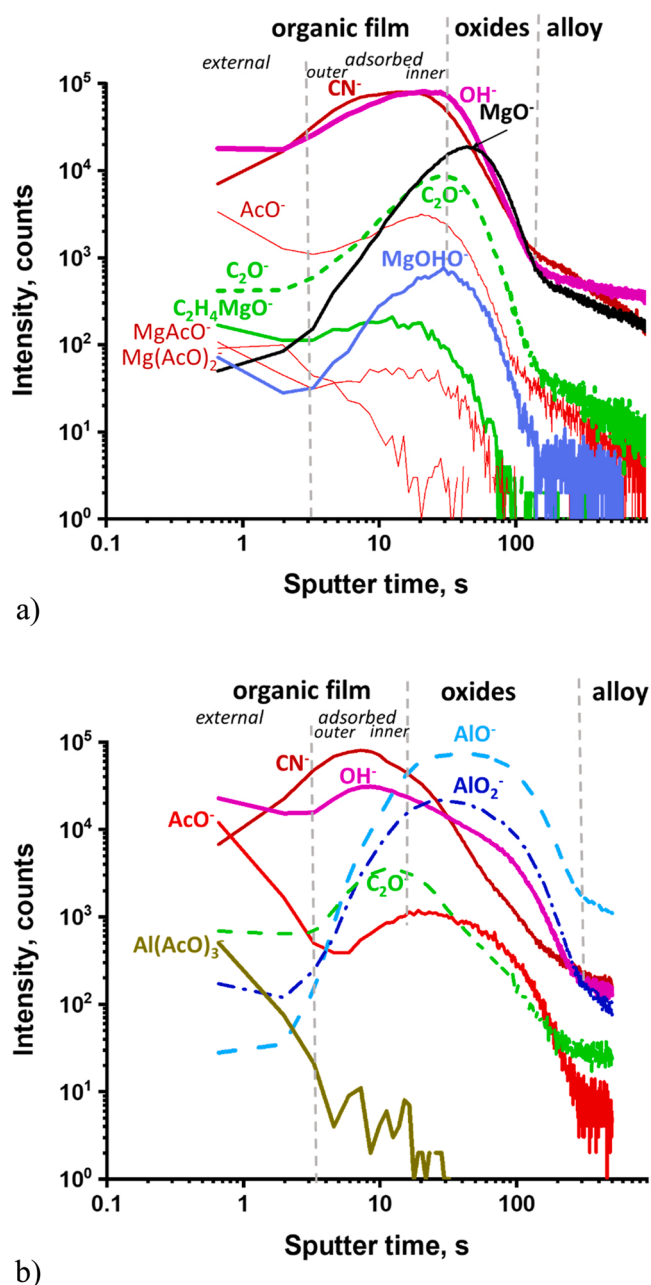


Fig. 7. Typical ToF-SIMS negative ions depth profiles obtained after electrochemical experiments in $[\text{mPEG}_n\text{MPyr}]\text{AcO}-\text{H}_2\text{O}$ electrolyte on (a) CP Mg and (b) CP Al. Tentative positions of the interfaces between the oxide layer and the sublayers of the surface film are shown by vertical lines.

Fig. 6 represents negative ions profile of the AZ61 sample after the electrochemical test. Two principal layers are distinguishable on the alloy: the organic species containing film and the oxide. The oxide layer contains Al and Mg oxides, marked by AlO^- and MgO^- fragments. The surface film can be divided into three sublayers. The inner sublayer closest to the oxide is characterized by the maxima of AlO_2^- , $\text{C}_2\text{H}_4\text{MgO}^-$, C_2O^- and OH^- signals. The intensity of the OH^- signal on AZ61 is lower than that observed on CP Mg, Fig. 7a (the peak maximum is about two times lower). Taking into account the absence of $\text{Mg}(\text{OH})_2$ – signal in the Raman and FTIR spectra and high sensitivity of ToF SIMS, it is impossible to exclude the presence of very small quantities of hydroxyl at the oxide-organic film interface. These species could however be present on the oxide surface before the experiment or could be formed after the electrochemical experiment inside the humid film. Considering the

difference in the peak maximum positions for CN^- and C_2O^- , the cation of the ILs seems to be oriented toward the surface by etheric groups. The outer part of the film corresponds to the maxima of the signals of CN^- , AcO^- ($m/z = 59$) and $\text{C}_2\text{H}_4\text{MgO}^-$, indicating the presence of the cation in a complex with Mg. The maximum of the CN^- signal is reached after a relatively long sputtering time (about 25 s). For comparison, on the CP Mg and the CP Al (Fig. 7) the maximum of the CN^- signal is reached after 5–10 s of sputtering. Longer erosion on the AZ61 indicates the presence of a thicker external layer on AZ61. This layer is marked with the signals of the fragments of Al complexes with acetate and etheric fragments ($\text{Al}(\text{AcO})_3$, MgAcO^- , and other fragments shown near the profiles and also reported in Table S4 in supplementary information. Such a chemistry of the fragments suggests a condensed film which structure is ensured by coordinated metal-organic complexes. This film can be associated with the dark barrier film reported in [37], visible under anodic polarization on AZ61 in $[\text{mPEG}_n\text{MPyr}]\text{AcO}-\text{H}_2\text{O}$. This condensed film is expected to block water diffusion to the metal and hence the HE reaction.

Fig. 7a displays the profiles obtained on the CP Mg. Erosion of the surface film is quicker, the maximum of the oxide layer (MgO^-) signal is reached after 50 s of sputtering, which is about twice shorter than for the AZ61. Similar to the AZ61 surface, two layers can be distinguished: a layer enriched by organic compounds and a Mg oxide film close to the metal. A closer look at the organic-rich region of the surface film shows that it can be divided into several parts too. The closest to the oxide inner layer can be defined by the maximum of MgH_2O^- and C_2O^- signals, which are assumed to correspond to $\text{Mg}(\text{OH})_2$ and etheric group fragments, respectively, also observed on Raman and ATR-FTIR spectra. This allows us to suspect that the cations of the IL are adsorbed on the crystals of $\text{Mg}(\text{OH})_2$. The outer sublayer is characterized by the signals of OH^- , CN^- and $\text{C}_2\text{H}_4\text{MgO}^-$. Three last signals can be also attributed to the fragments of the cation of the IL. The presence of $\text{C}_2\text{H}_4\text{MgO}^-$ fragments evidences the complexation of Mg-ions by etheric groups as it has been reported previously for dry PEG-containing ionic liquids [30]. As for the AZ61 surface, the cations of the ILs seem to be oriented toward the surface by etheric groups. The maximum of the CN^- signal is reached after a short erosion time, indicating that the external layer is very thin and could be interpreted as an adsorbed layer predominantly composed of Mg acetate (represented by the signals of $\text{C}_4\text{H}_6\text{MgO}_4^-$, $\text{Mg}(\text{AcO})_2^-$ and MgAcO^- and AcO^-). Further detailed analysis of the external layer is provided by the positive and negative MS in supporting information (see supplementary information Figs. S3 and S4, Tables S4 and S5).

Fig. 7b displays negative ions depth profiles of the CP Al after the electrochemical experiment in $[\text{mPEG}_n\text{MPyr}]\text{AcO}-\text{H}_2\text{O}$, in which almost no reactivity was observed. The analysis revealed that there are at least two principal layers on the metal: a film, rich in organic fragments and an oxide film. The oxide layer is represented by the peaks of AlO^- and AlO_2^- signals. The organic film contains both C_2O^- and AcO^- (CH_3COO^-) which indicates the presence of IL. The maximum of the signals of $\text{Al}(\text{AcO})_3^-$, CN^- and OH^- are close to the external top surface. The maximum of the AcO^- signal is deeper in the profile than the maximum of the C_2O^- signal which is a fragment of the etheric group. This order is opposite to the order observed on the CP Mg and AZ61 samples, indicating that acetate complexes with the CP Al surface is probably formed the first. It can be however seen from the positions of the maxima of signals of CN^- and C_2O^- that the orientation of the cation of the IL is the same on all the substrates - etheric groups are oriented toward the metallic surface. The complexes of Al detected on CP Al are similar to that observed on AZ61 (see supplementary information Fig. S3c, S4b, table S4, S5).

The comparison of the depth profiles of AZ61, CP Mg and CP Al shows that both Mg and Al participate in the formation of the complexes with anions and cations in the surface film, and that the thick condensed film is formed only if the combination of both metallic cations is present. This film also contains complexes with both the PEG-substituted cation and the acetic anion.

Considering the results of ToF-SIMS depth profiles, Raman and ATR-FTIR spectra, a tentative schematic representation of the surface film,

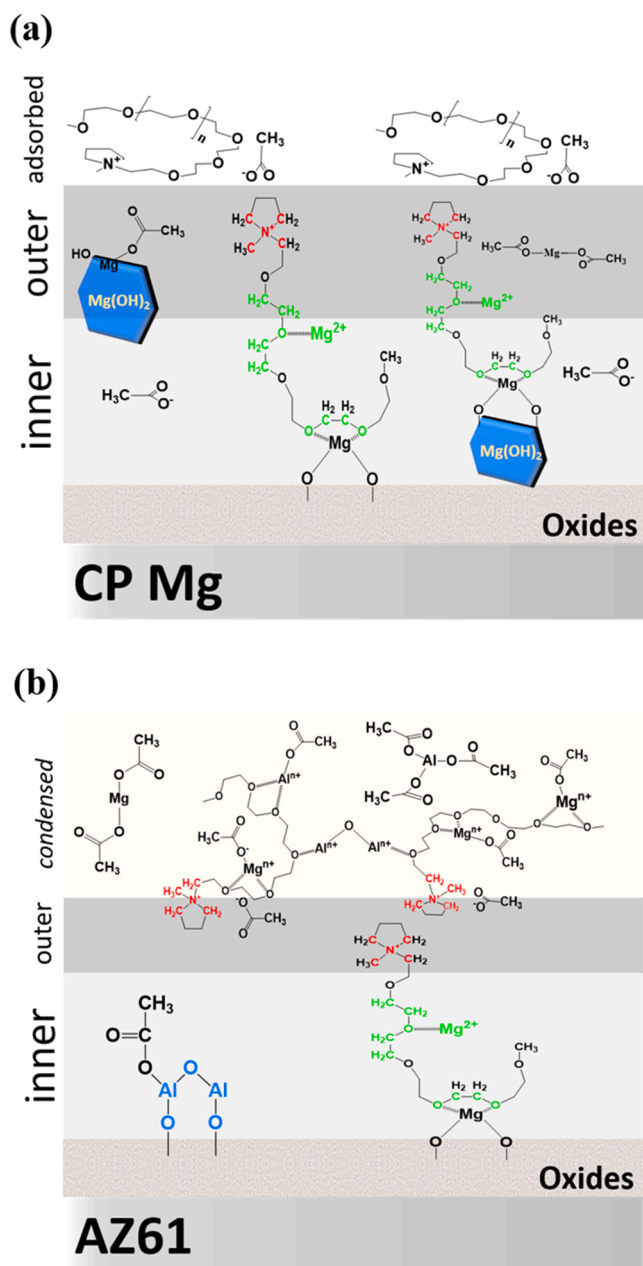


Fig. 8. Tentative schematics of the sublayers and interfaces observed in Fig. 4. The structures formed during anodic dissolution of (a) CP Mg and (b) AZ61 with [mPEG_nMPyr]AcO-water mixture are shown.

formed on Mg substrates in [mPEG_nMPyr]AcO-H₂O electrolyte can be proposed (Fig. 8). This schematic representation underlines that the surface of the CP Mg at some points is similar to that in aqueous electrolytes: the metallic surface is covered by MgO which is followed by Mg(OH)₂ [77]. Mg acetate and etheric groups are adsorbed on the hydroxide and the external cation head is responsible for the adsorption of acetate counter ions.

Mg(OH)₂ is detected only in trace quantities by ToF SIMS at the oxide-organic film interface on AZ61, which can be related to the oxide modification by Al [78,79]. In contrast, for the internal layer, in which the IL cations are fixed to the oxide by etheric groups, a relatively thick layer formed by Al- and Mg- complexes with cations and anions of the IL is condensed on the top of the external heterocycle oriented surface in place of adsorbed counter ions.

3.5. Molecular state of water molecules by ATR-FTIR

Molecular state of water in H₂O - IL mixtures can be understood by analyzing the evolution of the ATR-FTIR spectra in the region 3000 – 3700 cm⁻¹. Fig. 9 illustrates typical ATR-FTIR spectra of O-H vibration regions on the wet surfaces of the CP Mg and AZ61 samples compared with the spectra of pure water and the used electrolyte before and after the electrochemical experiments. Significant differences could be seen between the different electrolytes and the surfaces evolved in these electrolytes.

In [mPEG_nMPyr]ClO₄-H₂O and [mPEG_nMPyr]AcO-H₂O electrolytes a clear shoulder is visible nearby 3520–3530 cm⁻¹ but it is absent in [BMPyr]AcO-H₂O. In our previous work [63], the Raman peak at 3520 cm⁻¹ was attributed to specific interactions occurring when water molecules form H-bonds with etheric oxygen of the PEG-substituted cation and acetate anion (AcO...HOH...O_{etheric}). The hypothesis of H-bonds with etheric oxygen can also be confirmed in the present work by the spectrum of the [mPEG_nMPyr]ClO₄-H₂O electrolyte (Fig. 9 c, blue spectrum). The peak is even more pronounced however its position is shifted (≈3534 cm⁻¹) if compared to the [BMPyr]AcO-H₂O. This could be due to the fact that a weaker water and ClO₄ interaction, if compared with the water-acetate interaction, can contribute to the O-H vibrations of water, leading to a slight change of the peak center position [80].

On the metallic surfaces polarized in the [mPEG_nMPyr]AcO-H₂O electrolyte (Fig. 9 b), the shoulder at ≈ 3520 cm⁻¹ is present, indicating the interaction between water and etheric groups on the surface. This bonding of water can reduce its mobility and block its penetration to the metallic surface. Interestingly, on the CP Mg this effect seems to be more pronounced than on the AZ61 alloy. On the contrary, after the electrochemical experiments in [mPEG_nMPyr]ClO₄-H₂O, significant evolution of the spectra in the O-H region is visible both on the metallic surfaces and in the electrolyte (Fig. 9 c). Especially, on the CP Mg surface the spectrum approaches the spectrum of pure water. Thus, it can be assumed that after the reaction near the surface, the H-bonds between H₂O molecules and etheric oxygens in the cation are broken. Released water molecules are expected hence to form “free water” clusters. Another possible explanation is the decomposition of etheric groups [74].

The evolution of the bands describing H-bonds in water-water interactions allows also to verify the hypothesis that the “free water” phase formation in place of the initially H-bonded with acetate water molecules, which could be a consequence of stronger interactions between acetate anions and Mg²⁺ cations, leached by anodic reaction (1), than between acetate anions and water [63]. In the literature, the OH-bond oscillator strength is often correlated with the number of established H-bonds and hence the Gaussian components can be assigned to different populations of water molecules with different types/coordination [81]. The lowest frequency component of water spectra can be assigned to the water molecules participating in the percolating H-bonded water cluster or “free water” phase, as it is proposed in the literature [63,81]. It is clear from Fig. 9 that the contribution of “free” water does not increase on the surfaces polarized in the [mPEG_nMPyr]AcO-H₂O electrolyte (Fig. 9 b). The intensity of the lowest frequency shoulder, if compared to the bulk electrolyte, is significantly increased on the surfaces polarized in the [mPEG_nMPyr]ClO₄-H₂O (Fig. 9 c) or [BMPyr]AcO-H₂O (Fig. 9 a). There is hence a mechanism, by which the fraction of free water available for the electrochemical reactivity increases at the interface in these two electrolytes. This can be one of the reasons why anomalous hydrogen evolution is not suppressed in these electrolytes.

3.6. Molecular state of water molecules from MD simulations

ATR-FTIR spectroscopy demonstrated that for all the studied systems the fraction of free water at the interface is higher than in the bulk electrolyte. In order to further understand this phenomenon, MD

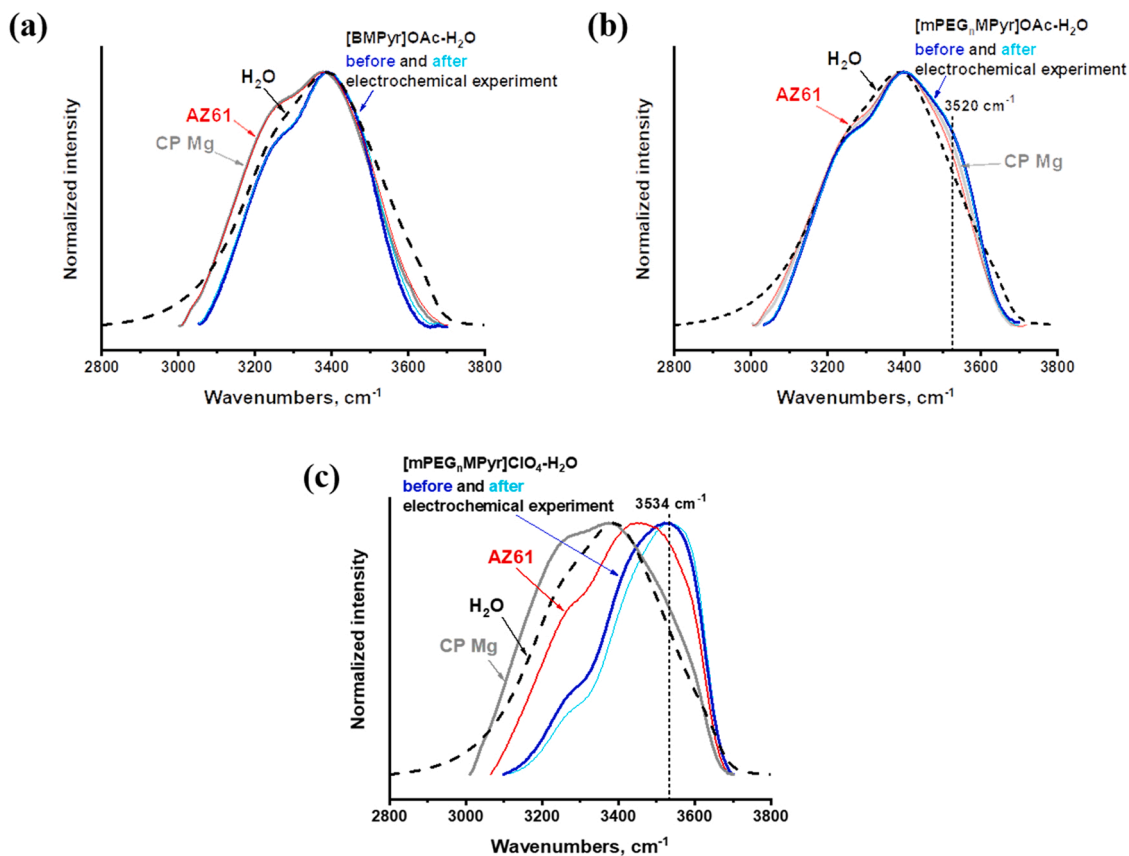


Fig. 9. Superposition of OH-vibration regions of ATR-FTIR spectra recorded on wet surfaces of CP Mg and AZ61 after the experiment in (a) - [BMPyr]AcO-H₂O; (b) - [mPEG_nMPyr]AcO-H₂O electrolyte; (c) - [mPEG_nMPyr]ClO₄-H₂O, as indicated. The spectra of pure water and of the electrolyte before and after the experiment are shown for comparison.

simulations were performed.

Preliminary MD simulation demonstrated that acetic anions can form strong intermolecular H-bonds with water, which is expected to prevent formation of free water phase [63] and hence to reduce hydrogen evolution in both [BMPyr]AcO-H₂O and [mPEG_nMPyr]AcO-H₂O. H-bonds were also demonstrated with etheric groups of the PEG substituted cation, but their probability for low water to IL molar ratios ($n(\text{H}_2\text{O}) / n(\text{IL}) \leq 3$) was lower than for the acetate anion. The probability of H-bonds between water molecules and acetate rapidly decreased with dilution, which could explain the effect of the electrolyte dilution on the NDE. However, the experiments in this work were made with a fixed water to IL molar ratio $n(\text{H}_2\text{O}) / n(\text{IL}) \leq 3$, at which water is bonded with acetate anion and hence the NDE suppression could be expected in both studied mixtures. This is however not the case in the electrochemical experiments. This can be regarded as an indication that “free” water forms at the interface between Mg alloy and the [BMPyr]AcO-H₂O electrolyte. The most probable reason is that some species, formed in the electrolyte because of Mg alloy degradation, could interact with both IL and water and interfere with water-IL interactions. The most probable species could be the Mg²⁺ ions leached by anodic dissolution (reaction 1).

This hypothesis is verified by considering the effect of Mg²⁺ on the stability of H-bonds between water and IL cations and anions in MD simulation. To this end, [BMPyr]AcO-H₂O and [mPEG_nMPyr]AcO-H₂O mixtures were simulated with and without Mg²⁺ (in the form of Mg(OH)₂ to ensure electro-neutrality and consider the most realistic system). In total 50 Mg²⁺ and OH⁻ couples were added in simulation box already containing 100 ion pairs (“molecules”) of the IL. Then, 100 or 200 water molecules were added to mimic the experimental molar ratios ($n(\text{H}_2\text{O})/n(\text{IL})$) of 1 and 2 respectively. Mg(OH)₂ as the source of Mg²⁺

in the simulation was selected because it is a common corrosion products of Mg-alloys, which is often naturally present in the outer layer on the metallic surface and was detected by Raman and IR spectroscopies on the CP Mg tested in all studied electrolytes. A slightly lower H₂O content than the experimentally used in the bulk electrolyte (theoretical molar ratio $n(\text{H}_2\text{O})/n(\text{IL}) = 2.9$ for [mPEG_nMPyr]AcO 10 wt% H₂O) was selected assuming a possible consumption of H₂O by the HE reaction (reaction 2) in open circuit periods and a limited diffusion of water to the interface.

$n(\text{H}_2\text{O}) / n(\text{IL}) = 2$ (red) are presented. Solid and dashed curves represent systems with and without addition of Mg ions respectively.

Examples of calculated radial distribution functions $G_r(r_{\text{HO-H}\cdots\text{O}_{\text{acetate}}})$ and $G_r(r_{\text{HO-H}\cdots\text{O}_{\text{etheric}}})$ are shown in Fig. 10. These functions describe the probability to find a H-atom from water a distance r to a specified oxygen which position is highlighted on the graphical formula in the figure. At large distances there is no interaction, so molecules are independent and $G(r) \sim 1$. For very small distances $G(r)$ is ~ 0 , reflecting the Pauli repulsion between atoms. The existence of specific interactions between atoms, e.g. hydrogen bonds between acetate anion, O_{acetate}, and water hydrogen atom H_{H₂O}, is reflected by the presence of one or more peaks. The position and the width of the peak identify the probability of the interaction. The effect of the addition of Mg²⁺ on the $G_r(r_{\text{HO-H}\cdots\text{O}_{\text{acetate}}})$ is depicted in Fig. 10 a for [BMPyr]AcO-H₂O and in Fig. 10 b for [mPEG_nMPyr]AcO-H₂O. In both cases $G_r(r_{\text{HO-H}\cdots\text{O}_{\text{acetate}}})$ is characterized by 2 peaks nearby 1.65 Å and 2.97 Å. In both electrolytes these peaks decrease in intensity with dilution and after addition of Mg²⁺, which could be due to the formation of Mg-acetate complexes.

In Fig. 10 c, the RDF of the 4th oxygen in polymeric chain is shown as an example of $G_r(r_{\text{HO-H}\cdots\text{O}_{\text{etheric}}})$. It is clear from this plot, that in contrast to $G_r(r_{\text{HO-H}\cdots\text{O}_{\text{acetate}}})$, for $G_r(r_{\text{HO-H}\cdots\text{O}_{\text{etheric}}})$ the addition of Mg²⁺

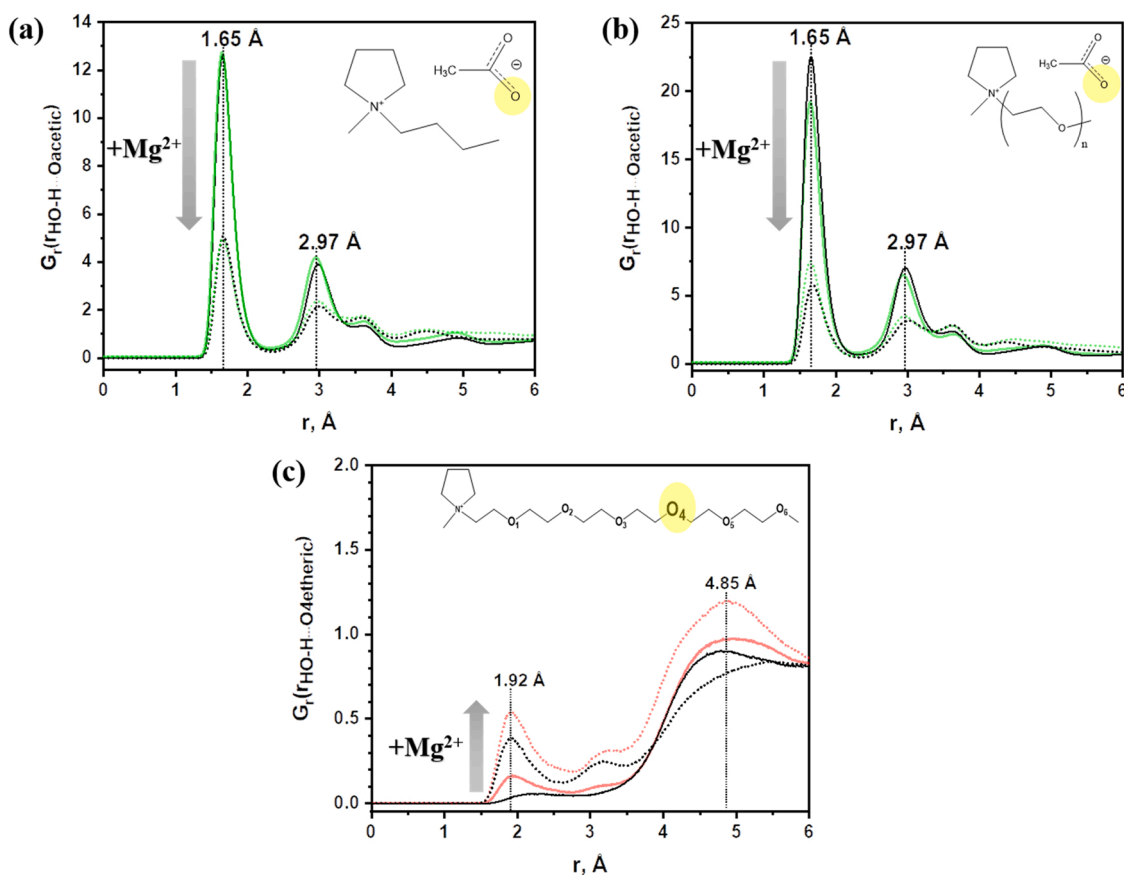


Fig. 10. Radial distribution functions $G_r(r_{\text{HO-H}\cdots\text{Oacetate}})$ (a, b) and $G_r(r_{\text{HO-H}\cdots\text{Oetheric}})$ (c) of the distances, r , between acetate oxygen or etheric oxygen 4 (shown in the insets) and the closest water hydrogen, calculated for water – [BMPyr]AcO (a) and water - [mPEG_nMPyr]AcO (b, c) mixtures without (solid lines) and with (dot lines) Mg^{2+} ions in solution. Examples of the mixtures with molar ratios between water and IL $n(\text{H}_2\text{O}) / n(\text{IL}) = 1$ (black) and.

increases the probability of H-bonding. Thus, it can be assumed that water molecules, expelled by Mg^{2+} from acetate anions, form hydrogen bonds with oxygen atoms of etheric groups of IL cation.

To illustrate the effect of Mg on all the etheric oxygen atoms, the difference of the RDF peak intensity with and without Mg-ions was

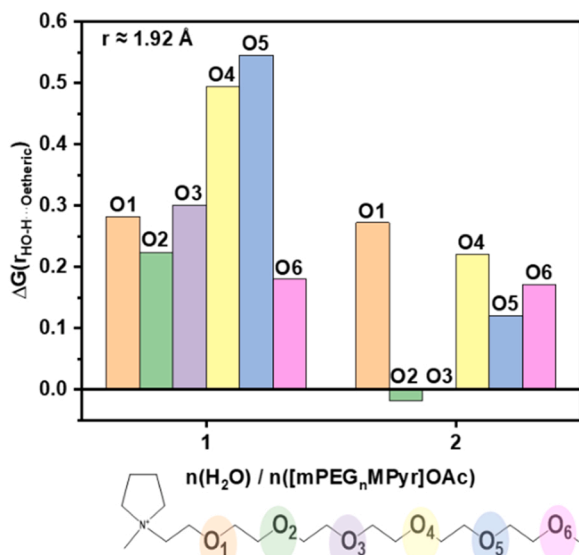


Fig. 11. Effect of leached Mg^{2+} ions in solution on the probability of water coordination by H-bonding with etheric oxygen atoms in water mixtures with different IL and molar water to IL ratios $n(\text{H}_2\text{O})/n(\text{IL})$ as indicated.

calculated. Fig. 11 represents the histograms of $\Delta G_r(r)$ for $\text{O}_{\text{etheric}}$ and $\text{H}_{(\text{H}_2\text{O})}$ for two mixtures (with the atomic ratios $n(\text{H}_2\text{O})/n(\text{IL}) = 1$ and 2). Positive values of $\Delta G_r(r_{\text{HO-H}\cdots\text{Oetheric}})$ for near all etheric oxygen positions indicate growing H-bonding probability with Mg^{2+} , however the magnitude of the effect depends on the O position and dilution. Interestingly, the effect of Mg^{2+} on O1 seems to be not affected by dilution.

4. Discussion: mechanisms of NDE and NDE-suppression on Mg alloys in H_2O -ILs mixtures

Whatever mechanism of the NDE is considered, it requires water reduction reaction (reaction 2) which needs the presence of the mobile free water phase which is not bonded with the IL. Comparing ATR-FTIR and molecular dynamic simulations results, one can conclude that water molecules in the bulk electrolytes can be strongly H-bonded by acetate anions in both [BMPyr]AcO- H_2O and [mPEG_nMPyr]AcO- H_2O mixtures with water to IL ratios $n(\text{H}_2\text{O})/n(\text{IL})$ up to 3 [63]. The results of the present work suggest that these $\text{HO-H}\cdots\text{O}_{\text{acetate}}$ bonds can be strongly weakened at the metal / solution interface because of the accumulation of Mg^{2+} leached by the anodic dissolution. As a result, in [BMPyr]AcO- H_2O mixture, a free water phase is present at the metal / solution interface and it is available for the HE reaction and hence also for the observed NDE. Moreover, the formed water phase is expected to be highly conductive because of the presence of dissolved acetate anions.

In the [mPEG_nMPyr]AcO- H_2O mixture, the water molecules, which were expelled from their H-bonds with acetate anions by the Mg^{2+} -ions leached from the alloys, seem to be immediately coordinated by etheric groups of the PEG-substituted cation. This H-bonding with the etheric oxygen seems to be even more probable with Mg^{2+} addition. Thus, water binding by the PEG substituted cation can be considered as one of the

mechanisms of the NDE inhibition, which is not expected to depend on the alloy composition.

One should note that the NDE was observed in the [mPEG_nMPyr] ClO₄-H₂O electrolyte (Section 3.2), which indicates that the inhibition in the [mPEG_nMPyr]AcO-H₂O is due to a synergic effect between the PEG-substituted cation and the carboxylic anion. The surface characterizations demonstrated partial transformation of etheric oxygen into C=O at the interface, probably also under the action of the electrochemically formed Mg²⁺ [74]. Strong bonding between Mg²⁺ and acetate anion can be the factor preventing PEG destabilization at the interface in [mPEG_nMPyr]AcO-H₂O electrolyte.

Finally, on the basis of ToF-SIMS, Raman and ATR-FTIR surface analysis, an additional NDE inhibition mechanism can be proposed which considers the effect of the condensed surface film which decreases mobility of water to the interface and hence the NDE. The formation of the film also requires the presence of both acetic anion and etherically substituted cation. The film composition and properties are therefore affected by the presence of both, Al and Mg, in the alloy.

It seems therefore that the NDE inhibition in [mPEG_nMPyr]AcO-H₂O electrolyte cannot be attributed solely to an anion or cation effect but is a result of a complex combination of synergic effects of both ions of the IL.

Fig. 12a and b illustrate schematically the proposed NDE mechanism on CP Mg and AZ61 alloys in [BMPyr]AcO-H₂O electrolyte. Dissolved Mg²⁺ ions expel H₂O molecules from acetic anions and released “free”

water molecules tend to form water-clusters involved in hydrogen reduction reaction.

In contrast, in the mixture [mPEG_nMPyr]AcO-H₂O (Fig. 12 c, d), the expelled H₂O molecules form intermolecular H-bonds with etheric oxygens of PEG-substituted cations, while leached Mg²⁺ ions participate in the formation of the surface film. This film composition is very different with and without Al³⁺. Formation of the condensed layer in the presence of Al³⁺ impedes the penetration of H₂O to the metallic surface. In addition, this film can level the electrochemical potential distribution at the interface thus preventing possible microgalvanic coupling caused by the substrates chemical inhomogeneity.

The proposed synergic inhibition mechanisms are depicted schematically in Fig. 12 and denoted by numbers 1 and 2. These mechanisms are the following: (1) ejection of water molecules from the acetate-water complexes by leached Mg²⁺ with the following formation of free water phase in the [BMPyr]AcO-H₂O mixture but immediate H-bonding of the formed water by [mPEG_nMPyr]⁺ and; 2) the barrier effect of the condensed film, in which [mPEG_nMPyr]⁺ and AcO⁻ moieties are initially coordinated by leached Mg²⁺ and Al³⁺ ions. Additional synergic effect is that the oxidation of [mPEG_nMPyr]⁺ by OH⁻ in presence of Mg²⁺ is prevented by the formation of soluble complexes between Mg²⁺ with acetate.

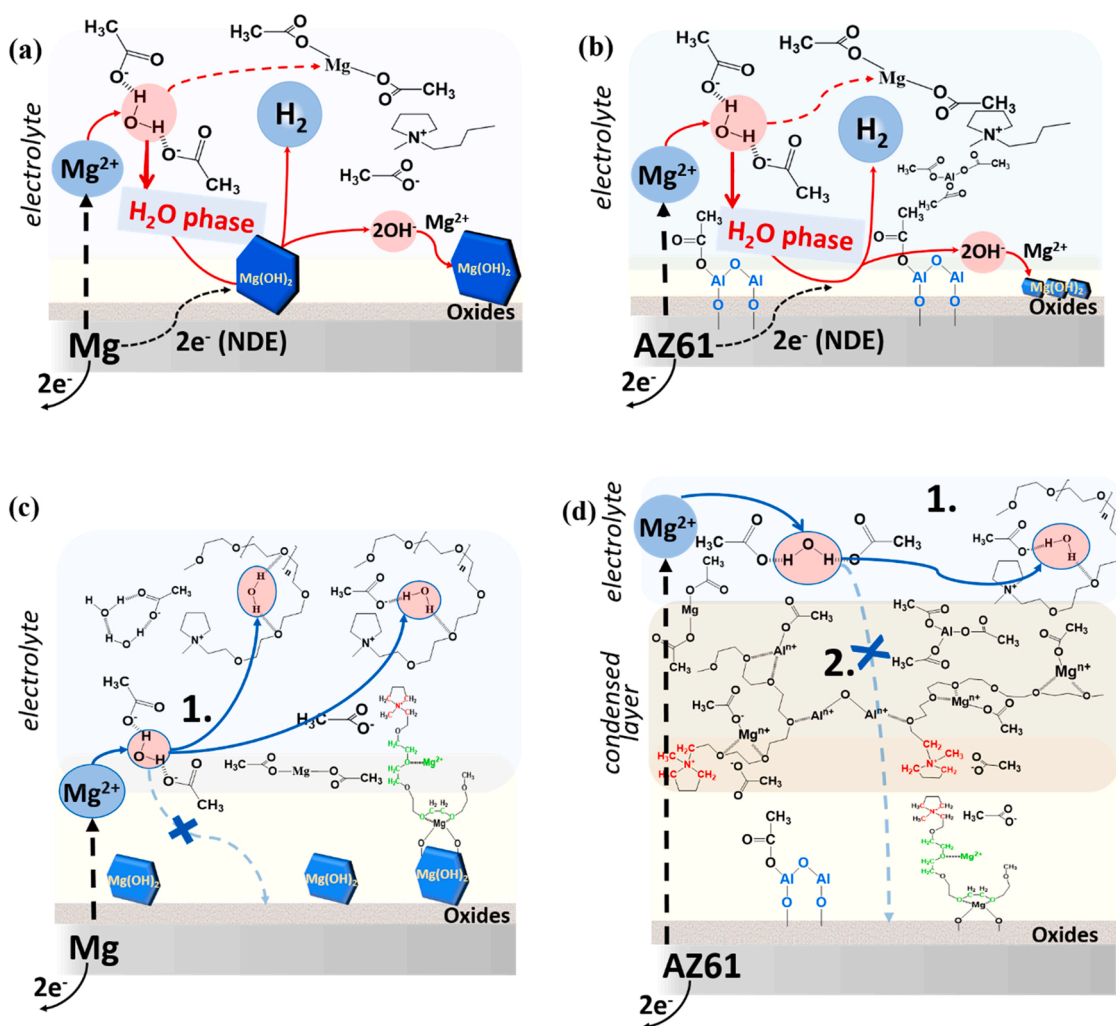


Fig. 12. Schematic mechanisms of NDE in [BMPyr]AcO-H₂O (a, b) and NDE inhibition in [mPEG_nMPyr]AcO-H₂O on CP Mg (c) and AZ61 (d). Numbers 1 and 2 indicate synergic inhibition mechanisms: 1. bonding by [mPEG_nMPyr]⁺ of free water phase, ejected from acetate-water H-bonded complexes by leached Mg²⁺; 2. barrier effect of the condensed film, in which [mPEG_nMPyr]⁺ and AcO⁻ moieties are coordinated by initially leached Mg²⁺ and Al³⁺ ions.

5. Conclusions

In this work the role of cations and anions of ionic liquids on the negative difference effect and its inhibition in water-ionic liquid mixtures was studied in detail considering as a typical example Mg alloys in [mPEG_nMPyr]ClO₄-H₂O, [BMPyr]AcO-H₂O and [mPEG_nMPyr]AcO-H₂O mixtures. Combining the results of our previous work [37] and the results obtained in this work, one can see the difference in the reactivity of Mg alloys in these electrolytes: the NDE occurs on CP Mg and AZ61 in the two first mixtures but does not on both alloys in [mPEG_nMPyr]AcO-H₂O, demonstrating a synergistic action of [mPEG_nMPyr]⁺ and AcO⁻.

Surface analysis by ToF-SIMS, surface and solution analysis by vibration spectroscopies combined with molecular dynamics simulations allow us to propose complementary mechanisms explaining the observed synergistic effect:

Effects in the electrolyte

Although water is H-bonded to the acetic anion in the bulk electrolyte, free water can be expelled from HO-H...AcO⁻ complexes by leached Mg²⁺. Thanks to the H-bonds between the released water and etheric oxygen atoms in [mPEG_nMPyr]⁺ its mobility and hence the electrochemical activity at the interface remains limited. The [mPEG_nMPyr]⁺ is however unstable in [mPEG_nMPyr]ClO₄-H₂O under anodic polarization because of nucleophilic attack by OH⁻ in the presence of Mg²⁺. AcO⁻ anions can bond leached Mg²⁺ forming strong acetate complexes, which stabilizes m-PEG substituted cation near the electrode.

Effects in the surface film

On AZ61, a condensed film can be formed by [mPEG_nMPyr]⁺ and AcO⁻ coordinated with Mg²⁺ and Al³⁺. This film is not very adherent but reforms spontaneously and can contribute to the decrease of the water transport to the surface.

To conclude, synergistic effect of acetic anions and ether-substituted pyrrolidinium cations can prevent the NDE on Mg in water-IL mixture.

CRedit authorship contribution statement

D. Kurchavov: Investigation, Methodology, Visualization, Validation, Data curation, Formal analysis, Writing – original draft, Writing – review & editing. **U. Rustambek:** Investigation, Validation. **A. Ottochian:** Supervision, Writing – review & editing. **G. Lefèvre:** Validation, Writing – review & editing. **A. Seyeux:** Investigation, Validation, Writing – review & editing. **I. Ciofini:** Validation, Writing – review & editing. **P. Marcus:** Validation, Writing – review & editing. **V. Lair:** Validation, Writing – review & editing. **P. Volovitch:** Conceptualization, Methodology, Validation, Visualization, Supervision, Writing – original draft, Writing – review & editing.

Declaration of Competing Interest

The authors declare that they have no known competing financial interests or personal relationships that could have appeared to influence the work reported in this paper.

Data availability

The raw/processed data required to reproduce these findings cannot be shared at this time due to technical or time limitations. They can be received by request.

Appendix A. Supporting information

Supplementary data associated with this article can be found in the

online version at doi:10.1016/j.corsci.2022.110723.

References

- [1] J. Tan, S. Ramakrishna, Applications of magnesium and its alloys: a review, Appl. Sci. (Switz.) 11 (2021), <https://doi.org/10.3390/app11156861>.
- [2] S. Sankaranarayanan, M. Gupta, Emergence of god's favorite metallic element: magnesium based materials for engineering and biomedical applications, Mater. Today Proc. 39 (2020) 311–316, <https://doi.org/10.1016/j.matpr.2020.07.220>.
- [3] R. Mohtadi, O. Tutusaus, T.S. Arthur, Z. Zhao-Karger, M. Fichtner, The metamorphosis of rechargeable magnesium batteries, Joule 5 (2021) 581–617, <https://doi.org/10.1016/j.joule.2020.12.021>.
- [4] M. Esmaily, J.E. Svensson, S. Fajardo, N. Birbilis, G.S. Frankel, S. Virtanen, R. Arrabal, S. Thomas, L.G. Johansson, Fundamentals and advances in magnesium alloy corrosion, Prog. Mater. Sci. 89 (2017) 92–193, <https://doi.org/10.1016/j.pmatsci.2017.04.011>.
- [5] E.J.F. Dickinson, A.J. Wain, The Butler-Volmer equation in electrochemical theory: origins, value, and practical application, J. Electroanal. Chem. 872 (2020), 114145, <https://doi.org/10.1016/j.jelechem.2020.114145>.
- [6] W. Beetz, XXXIV. On the development of hydrogen from the anode, Lond., Edinb., Dublin Philos. Mag. J. Sci. 32 (1866) 269–278, <https://doi.org/10.1080/14786446608644179>.
- [7] M. Deng, L. Wang, B. Vaghefiazari, W. Xu, C. Feiler, S.V. Lamaka, D. Höche, M. L. Zheludkevich, D. Snihirova, High-energy and durable aqueous magnesium batteries: Recent advances and perspectives, Energy Storage Mater. 43 (2021) 238–247, <https://doi.org/10.1016/j.ensm.2021.09.008>.
- [8] J. Huang, G.L. Song, A. Atrens, M. Dargusch, What activates the Mg surface—A comparison of Mg dissolution mechanisms, J. Mater. Sci. Technol. 57 (2020) 204–220, <https://doi.org/10.1016/j.jmst.2020.03.060>.
- [9] Y.L.G. Song, A. Atrens, D. Stjohn, J. Nairn, The electrochemical corrosion of pure magnesium in 1N NaCl, 39 (1997) 855–875, ([https://doi.org/10.1016/S0010-938X\(96\)00172-2](https://doi.org/10.1016/S0010-938X(96)00172-2)).
- [10] G. Song, A. Atrens, Understanding magnesium corrosion—a framework for improved alloy performance, Adv. Eng. Mater. 5 (2003) 837–858, <https://doi.org/10.1002/adem.200310405>.
- [11] Y. Li, Z. Shi, X. Chen, A. Atrens, Anodic hydrogen evolution on Mg, J. Magnes. Alloy. (2021), <https://doi.org/10.1016/j.jma.2021.09.002>.
- [12] W.D. Mueller, H. Hornberger, The influence of MgH₂ on the assessment of electrochemical data to predict the degradation rate of Mg and Mg alloys, Int. J. Mol. Sci. 15 (2014) 11456–11472, <https://doi.org/10.3390/ijms150711456>.
- [13] J. Chen, J. Dong, J. Wang, E. Han, W. Ke, Effect of magnesium hydride on the corrosion behavior of an AZ91 magnesium alloy in sodium chloride solution, Corros. Sci. 50 (2008) 3610–3614, <https://doi.org/10.1016/j.corsci.2008.09.013>.
- [14] G.L. Makar, J. Kruger, Corrosion studies of rapidly solidified magnesium alloys, J. Electrochem Soc. 137 (1990) 414–421, <https://doi.org/10.1149/1.2086455>.
- [15] G.L. Song, A. Atrens, Corrosion mechanisms of magnesium alloys, Adv. Eng. Mater. 1 (1999) 11–33, [https://doi.org/10.1002/\(SICI\)1527-2648\(199909\)1:1<11::AID-ADEM11>3.0.CO;2-N](https://doi.org/10.1002/(SICI)1527-2648(199909)1:1<11::AID-ADEM11>3.0.CO;2-N).
- [16] A. Atrens, G.L. Song, F. Cao, Z. Shi, P.K. Bowen, Advances in Mg corrosion and research suggestions, J. Magnes. Alloy. 1 (2013) 177–200, <https://doi.org/10.1016/j.jma.2013.09.003>.
- [17] S. Fajardo, G.S. Frankel, Effect of impurities on the enhanced catalytic activity for hydrogen evolution in high purity magnesium, Electro Acta 165 (2015) 255–267, <https://doi.org/10.1016/j.electacta.2015.03.021>.
- [18] G. Williams, H.Neil McMurray, Localized corrosion of magnesium in chloride-containing electrolyte studied by a scanning vibrating electrode technique, J. Electrochem Soc. 155 (2008) C340, <https://doi.org/10.1149/1.2918900>.
- [19] S. Thomas, N.V. Medhekar, G.S. Frankel, N. Birbilis, Corrosion mechanism and hydrogen evolution on Mg, Curr. Opin. Solid State Mater. Sci. 19 (2015) 85–94, <https://doi.org/10.1016/j.cossms.2014.09.005>.
- [20] D. Höche, C. Blawert, S.V. Lamaka, N. Scharnagl, C. Mendis, M.L. Zheludkevich, The effect of iron re-deposition on the corrosion of impurity-containing magnesium, Phys. Chem. Chem. Phys. 18 (2015) 1279–1291, <https://doi.org/10.1039/c5cp05577f>.
- [21] D. Mercier, J. Świątowska, S. Zanna, A. Seyeux, P. Marcus, Role of segregated iron at grain boundaries on Mg corrosion, J. Electrochem Soc. 165 (2018) C42–C49, <https://doi.org/10.1149/2.0621802jes>.
- [22] J.A. Yuwono, C.D. Taylor, G.S. Frankel, N. Birbilis, S. Fajardo, Understanding the enhanced rates of hydrogen evolution on dissolving magnesium, Electrochem Commun. 104 (2019), 106482, <https://doi.org/10.1016/j.elecom.2019.106482>.
- [23] M.J. Earle, J.M.S.S. Esperança, M.A. Gilea, J.N.C. Lopes, L.P.N. Rebelo, J. W. Magee, K.R. Seddon, J.A. Widegren, The distillation and volatility of ionic liquids, Nature 439 (2006) 831–834, <https://doi.org/10.1038/nature04451>.
- [24] P. Bonhte, A.P. Dias, N. Papageorgiou, K. Kalyanasundaram, M. Grätzel, Hydrophobic, highly conductive ambient-temperature molten salts, Inorg. Chem. 35 (1996) 1168–1178, <https://doi.org/10.1021/ic951325x>.
- [25] N. DeVos, C. Maton, C.V. Stevens, Electrochemical stability of ionic liquids: general influences and degradation mechanisms, ChemElectroChem 1 (2014) 1258–1270, <https://doi.org/10.1002/celec.201402086>.
- [26] G. Vardar, A.E.S. Sleightholme, J. Naruse, H. Hiramatsu, D.J. Siegel, C.W. Monroe, Electrochemistry of magnesium electrolytes in ionic liquids for secondary batteries, ACS Appl. Mater. Interfaces 6 (2014) 18033–18039, <https://doi.org/10.1021/am5049064>.
- [27] J.-A. Latham, P.C. Howlett, D.R. MacFarlane, A. Somers, M. Forsyth, Anodising AZ31 in a phosphonium ionic liquid: corrosion protection through composite film

- deposition, *J. Electrochem Soc.* 159 (2012) C539–C545, <https://doi.org/10.1149/2.015212jes>.
- [28] M. Forsyth, P.C. Howlett, S.K. Tan, D.R. MacFarlane, N. Birbilis, An ionic liquid surface treatment for corrosion protection of magnesium alloy AZ31, *Electrochem. Solid-State Lett.* 9 (2006) 52–55, <https://doi.org/10.1149/1.2344826>.
- [29] T. Watkins, A. Kumar, D.A. Buttry, Supporting information designer ionic liquids for reversible electrochemical deposition / dissolution of Mg, *J. Am. Chem. Soc.* 138 (2016) 1–9, <https://doi.org/10.1021/jacs.5b11031>.
- [30] X. Gao, A. Mariani, S. Jeong, X. Liu, X. Dou, M. Ding, A. Moretti, S. Passerini, Prototype rechargeable magnesium batteries using ionic liquid electrolytes, *J. Power Sources* 423 (2019) 52–59, <https://doi.org/10.1016/j.jpowsour.2019.03.049>.
- [31] A.M. O'Mahony, D.S. Silvester, L. Aldous, C. Hardacre, R.G. Compton, Effect of water on the electrochemical window and potential limits of room-temperature ionic liquids, *J. Chem. Eng. Data* 53 (2008) 2884–2891, <https://doi.org/10.1021/jc800678e>.
- [32] K.N. Marsh, J.A. Boxall, R. Lichtenthaler, Room temperature ionic liquids and their mixtures - A review, *Fluid Phase Equilib.* 219 (2004) 93–98, <https://doi.org/10.1016/j.fluid.2004.02.003>.
- [33] S. Fendt, S. Padmanabhan, H.W. Blanch, J.M. Prausnitz, Viscosities of acetate or chloride-based ionic liquids and some of their mixtures with water or other common solvents, *J. Chem. Eng. Data* 56 (2011) 31–34, <https://doi.org/10.1021/jc1007235>.
- [34] T. Zhang, Z. Tao, J. Chen, Magnesium-air batteries: from principle to application, *Mater. Horiz.* 1 (2014) 196–206, <https://doi.org/10.1039/c3mh00059a>.
- [35] Y. Zhang, R. Ye, D. Henkensmeier, R. Hempelmann, R. Chen, Water-in-ionic liquid solutions towards wide electrochemical stability windows for aqueous rechargeable batteries, *Electro Acta* 263 (2018) 47–52, <https://doi.org/10.1016/j.electacta.2018.01.050>.
- [36] A. Shkurankov, S. Zein El Abedin, F. Endres, AFM-assisted investigation of the corrosion behaviour of magnesium and AZ91 alloys in an ionic liquid with varying water content, *Aust. J. Chem.* 60 (2007) 35–42, <https://doi.org/10.1071/CH06305>.
- [37] D. Kurchavov, M. Haddad, V. Lair, P. Volovitch, Mg-alloys in water – hydrophilic ionic liquid mixtures: is there a negative difference effect, *Corros. Sci.* (2022), 110178, <https://doi.org/10.1016/j.corsci.2022.110178>.
- [38] S.V. Lamaka, B. Vaghefinazari, D. Mei, R.P. Petruskas, D. Höche, M. L. Zheludkevich, Comprehensive screening of Mg corrosion inhibitors, *Corros. Sci.* 128 (2017) 224–240, <https://doi.org/10.1016/j.corsci.2017.07.011>.
- [39] A. Maltseva, S.V. Lamaka, K.A. Yasakau, D. Mei, D. Kurchavov, M.L. Zheludkevich, G. Lefevre, P. Volovitch, In situ surface film evolution during Mg aqueous corrosion in presence of selected carboxylates, *Corros. Sci.* 171 (2020), 108484, <https://doi.org/10.1016/j.corsci.2020.108484>.
- [40] Y. Cui, T. Zhang, F. Wang, New understanding on the mechanism of organic inhibitors for magnesium alloy, *Corros. Sci.* (2022), 110118, <https://doi.org/10.1016/j.corsci.2022.110118>.
- [41] X. Liu, L. Hou, H. Wang, Y. Li, H. Wei, B. Liu, H. Du, Y. Wei, Synergistic inhibition behavior of sodium diethyldithiocarbamate and sodium acetate for AZ31B magnesium alloy in NaCl solution, *Mater. Express* 9 (2019) 27–41, <https://doi.org/10.1166/mex.2019.1472>.
- [42] E. Slavcheva, G. Schmitt, Screening of new corrosion inhibitors via electrochemical noise analysis, *Materials and Corrosion* 53 (2002) 647–655, [https://doi.org/10.1002/1521-4176\(200209\)53:9<647::AID-MAC0647>3.0.CO;2-L](https://doi.org/10.1002/1521-4176(200209)53:9<647::AID-MAC0647>3.0.CO;2-L).
- [43] X. Lu, Y. Li, P. Ju, Y. Chen, J. Yang, K. Qian, T. Zhang, F. Wang, Unveiling the inhibition mechanism of an effective inhibitor for AZ91 Mg alloy, *Corros. Sci.* 148 (2019) 264–271, <https://doi.org/10.1016/j.corsci.2018.12.025>.
- [44] D. Huang, J. Hu, G.L. Song, X. Guo, Inhibition effect of inorganic and organic inhibitors on the corrosion of Mg-10Gd-3Y-0.5Zr alloy in an ethylene glycol solution at ambient and elevated temperatures, *Electro Acta* 56 (2011) 10166–10178, <https://doi.org/10.1016/j.electacta.2011.09.002>.
- [45] Y. Liu, Z. Yu, S. Zhou, L. Wu, Self-assembled monolayers on magnesium alloy surfaces from carboxylate ions, *Appl. Surf. Sci.* 252 (2006) 3818–3827, <https://doi.org/10.1016/j.apsusc.2005.05.072>.
- [46] A. Mahapatro, T.D. Matos Negrón, A. Nguyen, Spectroscopic evaluations of interfacial oxidative stability of phosphonic nanocoatings on magnesium, *J. Spectrosc.* (2015) (2015), <https://doi.org/10.1155/2015/350630>.
- [47] M. Liu, S. Zanna, H. Ardelean, I. Frateur, P. Schmutz, G. Song, A. Atrens, P. Marcus, A first quantitative XPS study of the surface films formed, by exposure to water, on Mg and on the Mg-Al intermetallics: Al₃Mg₂ and Mg₁₇Al₁₂, *Corros. Sci.* 51 (2009) 1115–1127, <https://doi.org/10.1016/j.corsci.2009.02.017>.
- [48] P.C. Hidber, T.J. Graule, L.J. Gauckler, Citric acid - A dispersant for aqueous alumina suspensions, *J. Am. Ceram. Soc.* 79 (1996) 1857–1867, <https://doi.org/10.1111/j.1151-2916.1996.tb08006.x>.
- [49] R. Solmaz, G. Kardaş, B. Yazici, M. Erbil, Citric acid as natural corrosion inhibitor for aluminium protection, *Corros. Eng. Sci. Technol.* 43 (2008) 186–191, <https://doi.org/10.1179/174327807x214770>.
- [50] J. Wysocka, M. Cieslik, S. Krakowiak, J. Ryl, Carboxylic acids as efficient corrosion inhibitors of aluminium alloys in alkaline media, *Electro Acta* 289 (2018) 175–192, <https://doi.org/10.1016/j.electacta.2018.08.070>.
- [51] M.N. Moussa, M.M. El-Tagoury, A.A. Radi, S.M. Hassan, Carboxylic acids as corrosion inhibitors for aluminium in acidic and alkaline solutions, *Anti-Corros. Methods Mater.* 37 (1990) 4–8, <https://doi.org/10.1108/eb007262>.
- [52] P.S.D. Brito, C.A.C. Sequeira, Organic inhibitors of the anode self-corrosion in aluminum-air batteries, *J. Fuel Cell Sci. Technol.* 11 (2014) 1–10, <https://doi.org/10.1115/1.4025534>.
- [53] K.A. Yasakau, A. Maltseva, S.V. Lamaka, D. Mei, H. Orvi, P. Volovitch, M.G. S. Ferreira, M.L. Zheludkevich, The effect of carboxylate compounds on Volta potential and corrosion inhibition of Mg containing different levels of iron, *Corros. Sci.* 194 (2022), 109937, <https://doi.org/10.1016/j.corsci.2021.109937>.
- [54] D. Mercier, J. Światowska, E. Protopopoff, S. Zanna, A. Seyeux, P. Marcus, Inhibition of Mg corrosion by sulfur blocking of the hydrogen evolution reaction on iron impurities, *J. Electrochem Soc.* 167 (2020), 121504, <https://doi.org/10.1149/1945-7111/abaf79>.
- [55] P.C. Howlett, T. Khoo, G. Mooketsi, J. Efthimiadis, D.R. MacFarlane, M. Forsyth, The effect of potential bias on the formation of ionic liquid generated surface films on Mg alloys, *Electro Acta* 55 (2010) 2377–2383, <https://doi.org/10.1016/j.electacta.2009.11.080>.
- [56] M. Finšgar, Surface analysis of the 2-mercaptobenzothiazole corrosion inhibitor on 6082 aluminum alloy using ToF-SIMS and XPS, *Anal. Methods* 12 (2020) 456–465, <https://doi.org/10.1039/c9ay02293g>.
- [57] M. Esmaily, P. Malmberg, M. Shahabi-Navid, J.E. Svensson, L.G. Johansson, A ToF-SIMS investigation of the corrosion behavior of Mg alloy AM50 in atmospheric environments, *Appl. Surf. Sci.* 360 (2016) 98–106, <https://doi.org/10.1016/j.apsusc.2015.11.002>.
- [58] L. Cammarata, S.G. Kazarian, P.A. Salter, T. Welton, Molecular states of water in room temperature ionic liquids, *Phys. Chem. Chem. Phys.* 3 (2001) 5192–5200, <https://doi.org/10.1039/b106900d>.
- [59] M. Brehm, H. Weber, A.S. Pensado, A. Stark, B. Kirchner, Liquid structure and cluster formation in ionic liquid/water mixtures - An extensive ab initio molecular dynamics study on 1-ethyl-3-methylimidazolium acetate/water mixtures - Part 2, *Z. Fur Phys. Chem.* 227 (2013) 177–203, <https://doi.org/10.1524/zpch.2012.0327>.
- [60] Y. Chen, Y. Cao, Y. Zhang, T. Mu, Hydrogen bonding between acetate-based ionic liquids and water: three types of IR absorption peaks and NMR chemical shifts change upon dilution, *J. Mol. Struct.* 1058 (2014) 244–251, <https://doi.org/10.1016/j.molstruc.2013.11.010>.
- [61] O. Palumbo, F. Trequattrini, J.B. Brubach, P. Roy, A. Paolone, Molecular assembling in mixtures of hydrophilic 1-butyl-1-methylpyrrolidinium dicyanamide ionic liquid and water, *Appl. Sci. (Switz.)* 10 (2020), <https://doi.org/10.3390/app10144837>.
- [62] E.E. Fenn, D.E. Moilanen, N.E. Levinger, M.D. Fayer, Water dynamics and interactions in water–polyether binary mixtures, *J. Am. Chem. Soc.* 131 (2009) 5530–5539, <https://doi.org/10.1021/ja809261d>.
- [63] P. Volovitch, D. Kurchavov, U. Rustambek, M. Haddad, A. Ottochan, G. Lefevre, I. Ciofini, V. Lair, Influence of PEG-containing cation on molecular state of water in water – acetate based ionic liquids mixtures, *The Journal of Molecular Liquids* (2022), 120564, <https://doi.org/10.1016/j.molliq.2022.120564>.
- [64] L.V.N.R. Ganapatibhotla, J. Zheng, D. Roy, S. Krishnan, PEGylated imidazolium ionic liquid electrolytes: thermophysical and electrochemical properties, *Chem. Mater.* 22 (2010) 6347–6360, <https://doi.org/10.1021/cm102263s>.
- [65] D. Kasprzak, I. Stepniak, M. Galinski, Acetate- and lactate-based ionic liquids: synthesis, characterisation and electrochemical properties, *J. Mol. Liq.* 264 (2018) 233–241, <https://doi.org/10.1016/j.molliq.2018.05.059>.
- [66] M. Schmeisser, P. Illner, R. Puchta, A. Zahl, R. Van Eldik, Gutmann donor and acceptor numbers for ionic liquids, *Chem. - A Eur. J.* 18 (2012) 10969–10982, <https://doi.org/10.1002/chem.201200584>.
- [67] S. Plimpton, Fast parallel algorithms for short-range molecular dynamics, *J. Comput. Phys.* 117 (2008) 1–19.
- [68] L. Martínez, R. Andrade, E.G. Birgin, J.M. Martínez, Packmol: a package for building initial configurations for molecular dynamics simulations, *J. Comput. Chem.* 30 (2009) 2157–2164.
- [69] J. Wang, W. Wang, K.P. A, D.A. Case, Automatic atom type and bond type perception in molecular mechanical calculations, *J. Mol. Graph Model* 25 (2006) 247–260.
- [70] K. Yoshii, T. Uto, N. Tachikawa, Y. Katayama, The effects of the position of the ether oxygen atom in pyrrolidinium-based room temperature ionic liquids on their physicochemical properties, *Phys. Chem. Chem. Phys.* 22 (2020) 19480–19491, <https://doi.org/10.1039/d0cp02662j>.
- [71] C.J. Cramer, *Essentials of Computational Chemistry: Theories and Models*, 2nd ed., 2013, John Wiley & Sons, 2013.
- [72] M.J. Frisch, G.W. Trucks, H.B. Schlegel, G.E. Scuseria, M.A. Robb, J.R. Cheeseman, G. Scalmani, V. Barone, G.A. Petersson, X. Nakatsuji, H.; Li, M. Caricato, A.V. Marenich, J. Bloino, B.G. Janesko, R. Gomperts, B. Mennucci, D.J. Hratch, Gaussian 16, Revision C.01, Gaussian, Inc., Wallingford CT. (2016).
- [73] D. Brouillette, D.E. Irish, N.J. Taylor, G. Perron, M. Odziemkowski, J.E. Desnoyers, Stable solvates in solution of lithium bis(trifluoromethylsulfone)imide in glymes and other aprotic solvents: phase diagrams, crystallography and Raman spectroscopy, *Phys. Chem. Chem. Phys.* 4 (2002) 6063–6071, <https://doi.org/10.1039/b203776a>.
- [74] Y. Yu, A. Baskin, C. Valero-Vidal, N.T. Hahn, Q. Liu, K.R. Zavadil, B.W. Eichhorn, D. Prendergast, E.J. Crumlin, Instability at the electrode/electrolyte interface induced by hard cation chelation and nucleophilic attack, *Chem. Mater.* 29 (2017) 8504–8512, <https://doi.org/10.1021/acs.chemmater.7b03404>.
- [75] G. Lefevre, T. Preocanin, J. Lützenkirchen, Attenuated Total Reflection - Infrared Spectroscopy Applied to the Study of Mineral - Aqueous Electrolyte Solution Interfaces: A General Overview and a Case Study, *Infrared Spectroscopy - Materials Science, Engineering and Technology.* (2012). (<https://doi.org/10.5772/36459>).
- [76] A. Maltseva, V. Shkirskiy, G. Lefevre, P. Volovitch, Effect of pH on Mg(OH)₂ film evolution on corroding Mg by in situ kinetic Raman mapping (KRM), *Corros. Sci.* 153 (2019) 272–282, <https://doi.org/10.1016/j.corsci.2019.03.024>.

- [77] M. Taheri, R.C. Phillips, J.R. Kish, G.A. Botton, Analysis of the surface film formed on Mg by exposure to water using a FIB cross-section and, in: STEM (Ed.), Corros Sci, 59, 2012, pp. 222–228, <https://doi.org/10.1016/j.corsci.2012.03.001>.
- [78] S. Fajardo, J. Bosch, G.S. Frankel, Anomalous hydrogen evolution on AZ31, AZ61 and AZ91 magnesium alloys in unbuffered sodium chloride solution, Corros. Sci. 146 (2019) 163–171, <https://doi.org/10.1016/j.corsci.2018.10.039>.
- [79] P. Volovitch, M. Serdechnova, K. Ogle, Aqueous corrosion of Mg-Al binary alloys: roles of Al and Mg, Corrosion 68 (2012) 557–570, <https://doi.org/10.5006/i0010-9312-68-6-557>.
- [80] L. Cammarata, S.G. Kazarian, P.A. Salter, T. Welton, Molecular states of water in room temperature ionic liquids Electronic Supplementary Information available. See <http://www.rsc.org/suppdata/cp/b1/b106900d/>, Physical Chemistry Chemical Physics. 3 (2001) 5192–5200. (<https://doi.org/10.1039/b106900d>).
- [81] J.B. Brubach, A. Mermet, A. Filabozzi, A. Gerschel, P. Roy, Signatures of the hydrogen bonding in the infrared bands of water, J. Chem. Phys. 122 (2005), <https://doi.org/10.1063/1.1894929>.